Article

Developmental Cell

Centriolar CPAP/SAS-4 Imparts Slow Processive Microtubule Growth

Highlights

- CPAP's PN2-3 domain binds to an exposed site on β-tubulin at microtubule plus ends
- CPAP tracks and caps microtubule plus ends in vitro
- CPAP dampens microtubule growth in vitro
- The capping function of CPAP limits centriolar microtubule growth in human cells

Authors

Ashwani Sharma, Amol Aher, Nicola J. Dynes, ..., Anna Akhmanova, Pierre Gönczy, Michel O. Steinmetz

Correspondence

a.akhmanova@uu.nl (A.A.), pierre.gonczy@epfl.ch (P.G.), michel.steinmetz@psi.ch (M.O.S.)

In Brief

The mechanisms ensuring the extremely slow growth of centriolar microtubules remain elusive. Sharma, Aher, Dynes et al. demonstrate that human CPAP acts as a molecular lid that caps microtubule plus ends and dampens their elongation, thus contributing to centriole length control by ensuring slow processive assembly of centriolar microtubules.

Accession Numbers

5ITZ

Sharma et al., 2016, Developmental Cell *37*, 362–376
May 23, 2016
http://dx.doi.org/10.1016/j.devcel.2016.04.024

CellPress

CellPress

Developmental Cell
Article

Centriolar CPAP/SAS-4 Imparts Slow Processive Microtubule Growth

Ashwani Sharma,[1,5] Amol Aher,[2,5] Nicola J. Dynes,[3,5] Daniel Frey,[1] Eugene A. Katrukha,[2] Rolf Jaussi,[1] Ilya Grigoriev,[2] Marie Croisier,[4] Richard A. Kammerer,[1] Anna Akhmanova,[2,*] Pierre Gönczy,[3,*] and Michel O. Steinmetz[1,*]

[1]Laboratory of Biomolecular Research, Department of Biology and Chemistry, Paul Scherrer Institut, 5232 Villigen PSI, Switzerland
[2]Cell Biology, Faculty of Science, Utrecht University, 3584 CH Utrecht, The Netherlands
[3]Swiss Institute for Experimental Cancer Research (ISREC), School of Life Sciences, Swiss Federal Institute of Technology (EPFL), 1015 Lausanne, Switzerland
[4]Bio-EM Facility, School of Life Sciences, Swiss Federal Institute of Technology (EPFL), 1015 Lausanne, Switzerland
[5]Co-first author
*Correspondence: a.akhmanova@uu.nl (A.A.), pierre.gonczy@epfl.ch (P.G.), michel.steinmetz@psi.ch (M.O.S.)
http://dx.doi.org/10.1016/j.devcel.2016.04.024

SUMMARY

Centrioles are fundamental and evolutionarily conserved microtubule-based organelles whose assembly is characterized by microtubule growth rates that are orders of magnitude slower than those of cytoplasmic microtubules. Several centriolar proteins can interact with tubulin or microtubules, but how they ensure the exceptionally slow growth of centriolar microtubules has remained mysterious. Here, we bring together crystallographic, biophysical, and reconstitution assays to demonstrate that the human centriolar protein CPAP (SAS-4 in worms and flies) binds and "caps" microtubule plus ends by associating with a site of β-tubulin engaged in longitudinal tubulin-tubulin interactions. Strikingly, we uncover that CPAP activity dampens microtubule growth and stabilizes microtubules by inhibiting catastrophes and promoting rescues. We further establish that the capping function of CPAP is important to limit growth of centriolar microtubules in cells. Our results suggest that CPAP acts as a molecular lid that ensures slow assembly of centriolar microtubules and, thereby, contributes to organelle length control.

INTRODUCTION

Centrioles are evolutionarily conserved organelles that are pivotal for the formation of cilia, flagella, and centrosomes, and are thus critical for fundamental cellular processes such as signaling, polarity, motility, and division (reviewed in Azimzadeh and Marshall, 2010; Bornens, 2012; Jana et al., 2014; Gönczy, 2012). Owing to their central role in such diverse cellular processes, centriole aberrations contribute to a range of severe human diseases, including ciliopathies, primary microcephaly, and cancer (reviewed in Nigg and Raff, 2009; Gönczy, 2015). Microtubules are the major constituent of centrioles and are arranged in a radial nine-fold symmetrical array, typically of triplet microtubules, which forms a barrel-shaped centriolar wall (reviewed in Azimzadeh and Marshall, 2010; Bornens, 2012; Jana et al., 2014; Gönczy, 2012). Centriolar microtubules are unique in exhibiting exceptionally slow growth rates of a few tens of nanometers per hour on average, and in being very stable after their formation (Kuriyama and Borisy, 1981; Chretien et al., 1997). Such properties likely contribute to setting centriole length, which is well conserved across evolution. The behavior of centriolar microtubules is in stark contrast to that of their cytoplasmic counterparts, which assemble up to four orders of magnitude faster and are highly dynamic (Kinoshita et al., 2001). The molecular mechanisms that impart the exceptional slow growth rate and stability of centriolar microtubules are not known.

Several centriolar proteins that can directly interact with tubulin and/or microtubules have been identified, including CEP120, CEP135, Centrobin, and CPAP (Gudi et al., 2011; Lin et al., 2013a, 2013b; Hsu et al., 2008). CPAP (SAS-4 in worms and flies) is of particular interest, since it is the only component among the ones listed above that is present and essential for centriole formation from worm to man (Kohlmaier et al., 2009; Schmidt et al., 2009; Tang et al., 2009; Kirkham et al., 2003; Leidel and Gönczy, 2003). The importance of CPAP is further substantiated by the fact that homozygous mutations in the corresponding gene lead to autosomal recessive primary microcephaly, a devastating human disease with drastically reduced neuron numbers and, thus, brain size (Bond et al., 2005). Interestingly, CPAP overexpression induces overly long centrioles in human cells (Kohlmaier et al., 2009; Schmidt et al., 2009; Tang et al., 2009), thus interfering with cell division (Kohlmaier et al., 2009). Together, these observations suggest that CPAP somehow regulates centriolar microtubule growth to produce proper centrioles. How this role is exerted at a mechanistic level remains elusive.

CPAP comprises a tubulin-binding domain (PN2-3), a positively charged microtubule-binding domain (MBD), a coiled-coil dimerization domain, and a C-terminal G box (Figure 1A). The PN2-3 domain is of prime interest as this region is highly conserved across evolution and found exclusively in CPAP/SAS-4 proteins. PN2-3 sequesters tubulin dimers and has been shown to destabilize microtubules both in vitro and in cells (Hsu et al., 2008; Cormier et al., 2009; Hung et al., 2004). How this observation can be reconciled with the presence of overly

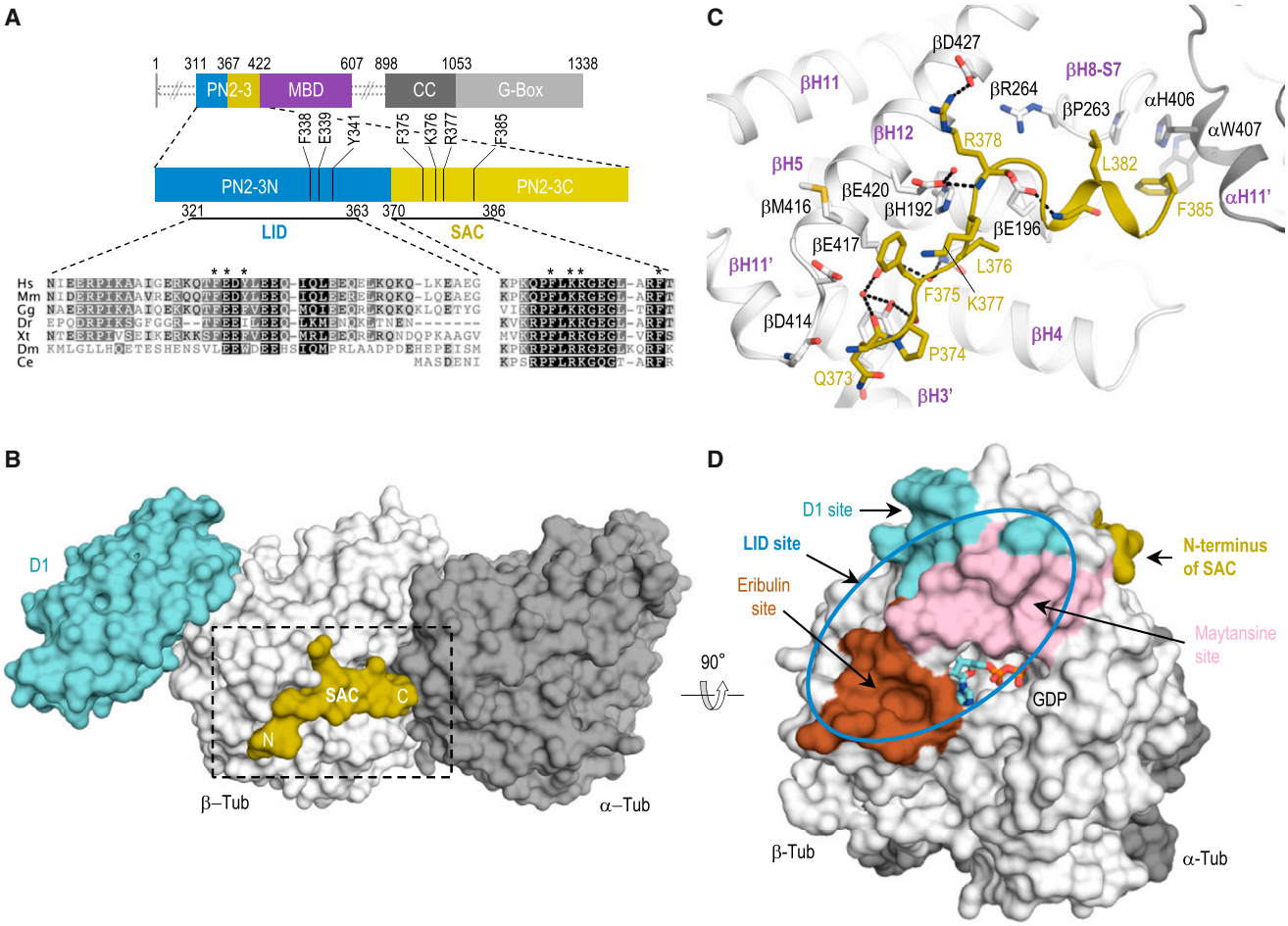

Figure 1. Structure of the Tubulin-PN2-3 Complex

(A) Domain organization of human CPAP, with indication of amino acid numbers at domain boundaries. The PN2-3 region is shown magnified below, with residue conservation among CPAP/SAS-4 proteins in *Homo sapiens*, *Mus musculus*, *Gallus gallus*, *Danio rerio*, *Xenopus tropicalis*, *Drosophila melanogaster*, and *Caenorhabditis elegans*. Black and gray shadings indicate different degrees of residue conservation. Blue and olive bars highlight the LID and SAC domains, respectively. Asterisks indicate residues that have been mutated in this study. MBD, microtubule-binding domain; CC, coiled coil.

(B) Overall view of the complex formed between PN2-3 (SAC residues in olive), αβ-tubulin (gray), and D1 (cyan). The N and C termini of SAC are indicated. The dashed box depicts the area shown in (C).

(C) Close-up view of the interaction between SAC (olive sticks) and tubulin (gray). Selected secondary structural elements of tubulin are labeled in bold purple letters. Residues at the tubulin-SAC interface are labeled in black and olive (SAC).

(D) Location of the D1 (cyan), eribulin (brown), and maytansine sites (pink) on β-tubulin. Note that eribulin binds to the vinca site on β-tubulin. The N terminus of SAC (olive) is shown. The blue oval represents the expected binding region of LID.

See also Tables S1 and S2.

long centrioles upon CPAP overexpression, which is suggestive of the protein-enhancing centriolar microtubule elongation, has remained puzzling. Here, to elucidate the fundamental mechanism of action of CPAP/SAS-4 proteins, we set out to decipher how CPAP affects microtubules using structural, biophysical, and cell biological approaches. We first report a high-resolution structure of αβ-tubulin in complex with the PN2-3 domain of CPAP. This structural information guided the design of experiments aimed at understanding the key role of CPAP in regulating centriolar microtubule behavior. Using reconstitution experiments, we demonstrate that CPAP autonomously recognizes and tracks growing microtubule plus ends. There, CPAP suppresses microtubule polymerization and increases microtubule stability by inhibiting catastrophes and promoting rescues. We further establish that the PN2-3 domain of CPAP is critical in the cellular context to restrict the extent of centriolar microtubule elongation by acting as a molecular "cap."

RESULTS

Crystal Structure of the SAC Domain of CPAP in a Complex with Tubulin

To gain insight into the molecular mechanism of tubulin binding by CPAP/SAS-4 proteins, we sought to crystallize the PN2-3 domain of human CPAP in complex with tubulin (see Table S1 for all constructs generated in the course of this study). Extensive crystallization trials with complexes of tubulin and PN2-3 variants were not met with success. However, adding the

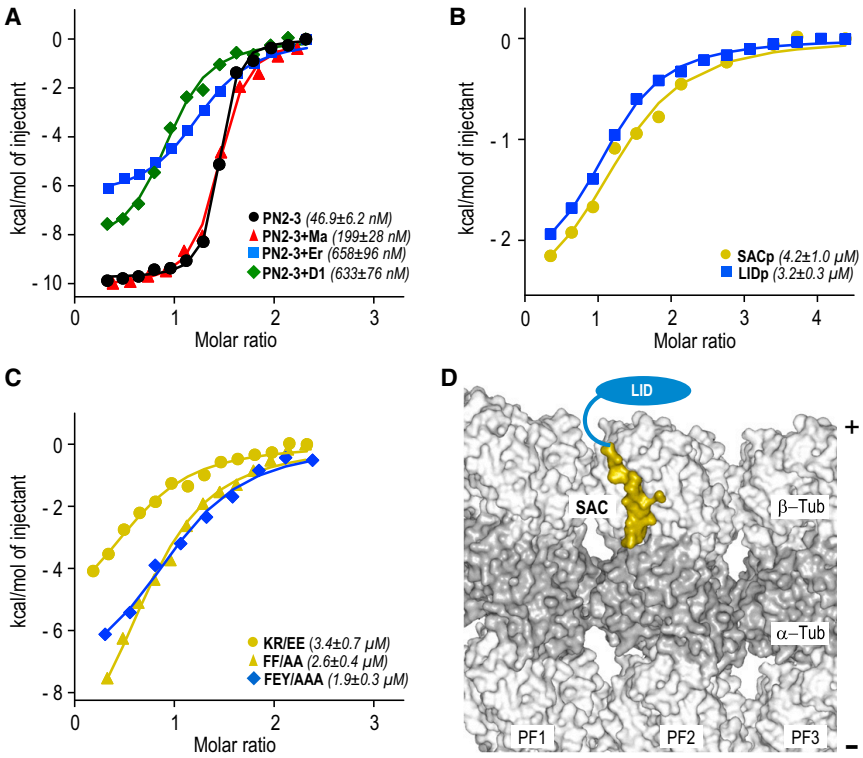

Figure 2. Interactions of PN2-3 with Tubulin and Microtubules

(A–C) ITC analysis of interactions between indicated PN2-3 variants and tubulin. D1, DARPin; Er, eribulin; Ma, maytansine. Note that eribulin and maytansine bind to the vinca site and maytansine site on β-tubulin, respectively (Gigant et al., 2005; Prota et al., 2014; Smith et al., 2010).

(D) Binding of SAC (olive surface representation) and LID (schematically represented by a blue oval) in the context of a microtubule plus end, with three protofilaments (PF1–PF3) being represented. Light-gray surface representation, β-tubulin; dark-gray surface representation, α-tubulin. The plus (+) and minus (–) ends of the microtubule are indicated on the right.

See also Figure S1 and Table S1.

β-tubulin-binding darpin (D1; Pecqueur et al., 2012) allowed us to solve the ternary complex formed between PN2-3, αβ-tubulin, and D1 (denoted the D1-tubulin-PN2-3 complex) to 2.2 Å resolution by X-ray crystallography (Figures 1A–1C and Table S2). As reported previously for other structures, the D1 molecule was bound at the tip of β-tubulin in the D1-tubulin-PN2-3 complex structure, a location involved in longitudinal tubulin-tubulin contacts within microtubules (Pecqueur et al., 2012). In addition, we found electron densities for residues 373–385 of PN2-3, which correspond to the evolutionarily conserved SAC domain of CPAP (for "Similar in SAS-4 and CPAP"; Leidel and Gönczy, 2003; Hsu et al., 2008; Kitagawa et al., 2011) (Figure 1B). In the PN2-3-tubulin-D1 complex structure, we found that SAC residues are engaged with both α- and β-tubulin subunits without affecting the overall conformation of the dimer (root-mean-square deviation of tubulin in the tubulin-D1 [PDB: 4DRX] and PN2-3-tubulin-D1 complex structures: 0.49 Å over 760 Cα atoms). The SAC-binding site on tubulin is shaped by hydrophobic and polar residues of helices αH11′, βH3′, βH5, and βH12, and loops βH8-S7 and βH11′-H12 (Figure 1C).

The SAC-tubulin interaction is characterized by an extensive water and non-water-mediated hydrogen-bonding network, as well as by hydrophobic contacts established between both main-chain and side-chain atoms of SAC and tubulin residues. Prominent SAC side-chain contacts involve Phe375 (βAsp414, βMet416, βGlu417, βGlu420), Leu376 (βHis192, βQln193, βGlu196), Lys377 (βGlu420), Arg378 (βGlu420, βAsn426), and Phe385 (αH406, αTrp407, βPro263). Pull-down experiments had implicated Lys377 and Arg378 in tubulin binding (Hsu et al., 2008), and our findings reveal the structural basis for their importance in this interaction.

Atomic Model of the Interaction of Tubulin and PN2-3

Previous studies suggested that PN2-3 inhibits exchange of the nucleotide on β-tubulin and that residues situated N-terminal to SAC also interact with tubulin (Cormier et al., 2009; Hsu et al., 2008; Hung et al., 2004). The D1-PN2-3-tubulin structure revealed that the N terminus of SAC is located close to the D1-binding site at the tip of β-tubulin (Figure 1D). We therefore reasoned that the presence of D1 might hinder access of this region of CPAP to its binding site. Accordingly, isothermal titration calorimetry (ITC) experiments demonstrated that whereas PN2-3 bound tubulin with an equilibrium dissociation constant (K_D) of 47 ± 6 nM, the affinity of PN2-3 for tubulin-D1 dropped one order of magnitude (Figure 2A). Likewise, eribulin and maytansine, two drugs that bind near the D1- and nucleotide-binding site, and which also inhibit longitudinal tubulin-tubulin contacts in microtubules (Pecqueur et al., 2012; Prota et al., 2014; Alday and Correia, 2009), significantly impaired the affinity of PN2-3 for tubulin (Figure 2A). We conclude that the N-terminal part of PN2-3 binds to a site on the tip of β-tubulin engaged in longitudinal tubulin-tubulin interactions (Cormier et al., 2009); we therefore named this putative domain "LID". To test whether the hydrolysis state of the exchangeable nucleotide bound to β-tubulin is important for tubulin-PN2-3 complex formation, as previously suggested for PN2-3 of *Drosophila* DmSAS-4 (Gopalakrishnan et al., 2012), we performed additional ITC experiments. As shown in Figure S1, we found similar K_D values for the interaction between human CPAP PN2-3 and guanosine diphosphate (GDP)-, guanosine triphosphate (GTP)-, or GMPCPP-tubulin (maximal difference of 1.3-fold). We conclude that the hydrolysis state of the nucleotide bound to β-tubulin has at most a minor effect on tubulin-PN2-3 complex formation.

To assess whether SAC and LID can bind tubulin independently, we generated two corresponding peptides, SACp and LIDp, and analyzed their tubulin-binding properties by ITC. K_D values in the low micromolar range were obtained for the interactions between tubulin and either SACp or LIDp (Figure 2B). To investigate the importance of selected SAC and LID residues

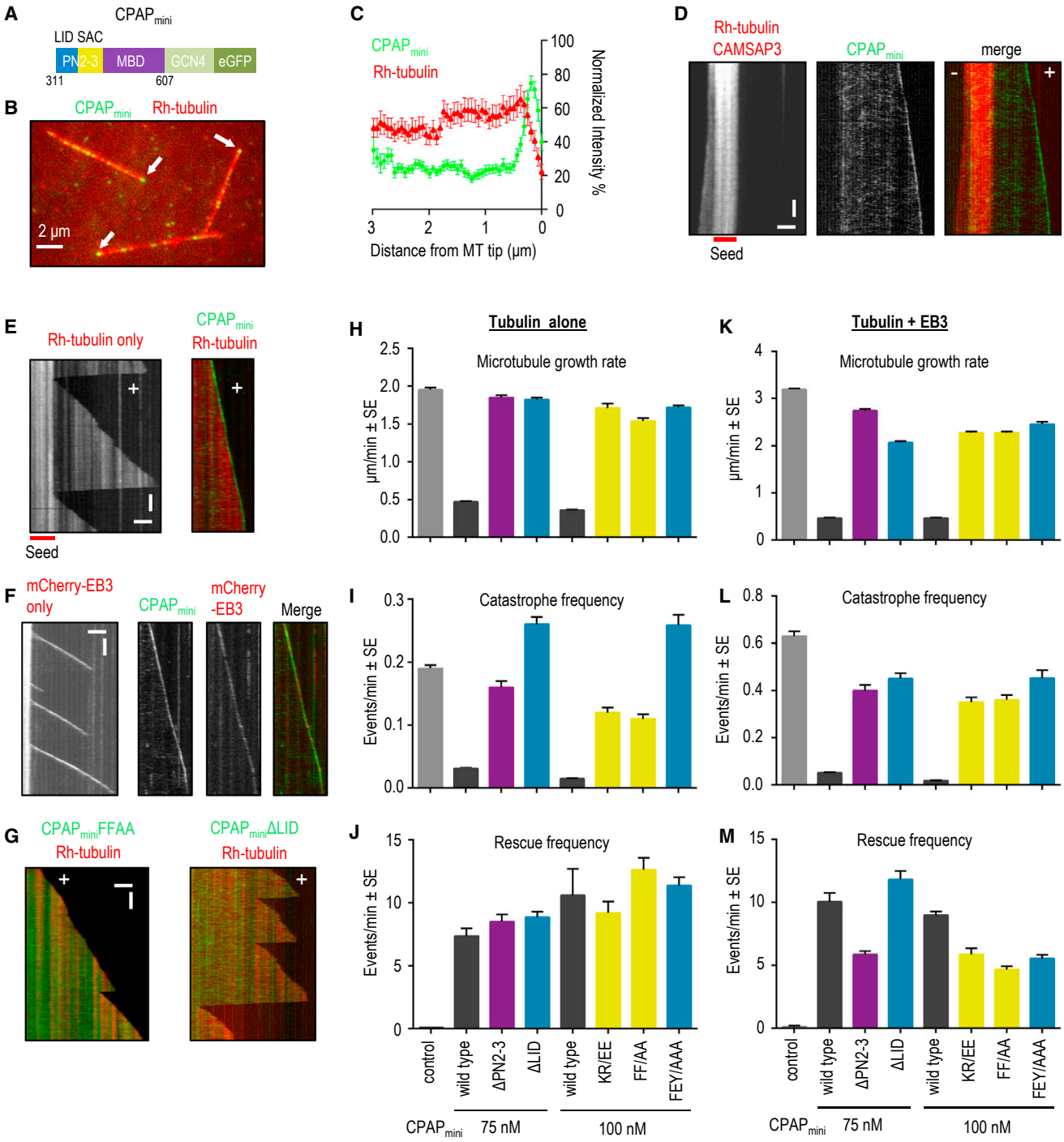

Figure 3. Effects of CPAP$_{mini}$ on Dynamic Microtubules

(A) Schematic of CPAP$_{mini}$ construct.

(B) Single frame of a time-lapse movie of rhodamine (Rh)-labeled microtubules growing from rhodamine-GMPCPP seeds in the presence of CPAP$_{mini}$. Arrows point to CPAP$_{mini}$ microtubule tip accumulation.

(C) Normalized mean intensity profiles for CPAP$_{mini}$ and rhodamine-tubulin obtained from 30 microtubules. Error bars represent SEM.

(D) Kymographs of microtubule growth at the plus (+) and minus (−) end from a rhodamine-GMPCPP seed with 50 nM mCherry-CAMSAP3 and 100 nM CPAP$_{mini}$.

(E) Kymographs of microtubule plus-end dynamics with rhodamine-tubulin alone or together with 100 nM CPAP$_{mini}$.

(F) Kymographs of microtubule plus-end dynamics with 20 nM mCherry-EB3 alone or together with 100 nM CPAP$_{mini}$.

(G) Kymographs of microtubule plus-end dynamics with rhodamine-tubulin and 100 nM of the two indicated CPAP$_{mini}$ variants.

(legend continued on next page)

for tubulin binding, we conducted further ITC experiments with mutant variants of the PN2-3 domain. Mutation of the tubulin-interacting SAC residues Lys377 and Arg378 to glutamic acid (KR/EE), or of Phe375 and Phe385 to alanine (FF/AA), reduced the affinity of PN2-3 for tubulin by two orders of magnitude (Figure 2C; compare with wild-type PN2-3 in Figure 2A). We also tested a PN2-3 mutant in which three residues in a conserved region of LID (Phe338, Glu339, Tyr341; Figure 1A) were simultaneously mutated to alanine (FEY/AAA), and also in this case obtained a K_D in the low micromolar range (Figure 2C).

These results suggest that both SAC and LID can bind independently to tubulin with low micromolar affinities, and that they cooperate to give rise to a ~100-fold tighter interaction with tubulin when present together. To test whether SAC and LID could bind in the context of microtubules, we used an atomic model of a microtubule based on a cryoelectron microscopy reconstruction at 3.5-Å resolution (Zhang et al., 2015). Interestingly, this analysis showed that both SAC and LID binding interfaces are located on the outer surface, at the distal tip of the microtubule, which has exposed β-tubulin subunits (Figure 2D). This result indicates that CPAP could specifically target microtubule plus ends via its PN2-3 domain.

CPAP Tracks Growing Microtubule Plus Ends In Vitro

To test the idea that CPAP targets microtubule plus ends, we performed in vitro reconstitution experiments whereby dynamic microtubules were grown from GMPCPP-stabilized seeds and imaged using a total internal reflection fluorescence (TIRF) microscopy-based assay (Bieling et al., 2007; Montenegro Gouveia et al., 2010). Since purified full-length CPAP was insoluble in our hands, we engineered a soluble chimeric protein in which the PN2-3-MBD moiety was fused to the leucine zipper domain of the yeast transcriptional activator GCN4 (O'Shea et al., 1991) to mimic the dimerization imparted by the endogenous coiled-coil domain of CPAP (Zhao et al., 2010), which is required for CPAP function in centriole duplication (Kitagawa et al., 2011), as well as to GFP (the resulting protein has been dubbed $CPAP_{mini}$; Figures 3A and S2A).

We found that $CPAP_{mini}$ bound weakly to the microtubule lattice; importantly, in addition, we found that $CPAP_{mini}$ localized to, and tracked, one end of dynamic microtubules specifically (Figures 3B–3E). We determined that $CPAP_{mini}$ bound the plus end of microtubules, distinguished as such because it is negative for the minus-end targeting protein CAMSAP3 (Figure 3D) (Jiang et al., 2014). $CPAP_{mini}$ co-localized at growing microtubule tips with the plus-end tracking protein EB3 (Figure 3F). However, in contrast to EB3, the plus-end accumulation of which critically depends on microtubule growth (Bieling et al., 2007; Montenegro Gouveia et al., 2010), $CPAP_{mini}$ was enriched at one end of GMPCPP-stabilized microtubules even when soluble tubulin was present at a concentration insufficient for microtubule elongation (5 instead of 15 μM tubulin; Figure S2B). These data reveal that microtubule growth is not required for plus-end recognition by $CPAP_{mini}$. In the absence of soluble tubulin, $CPAP_{mini}$ localized along the entire length of GMPCPP-stabilized microtubules (data not shown), indicating that the interaction of $CPAP_{mini}$ with soluble tubulin suppresses its binding to the microtubule lattice. Overall, we conclude that $CPAP_{mini}$ is an autonomous microtubule plus-end tracking protein.

CPAP Promotes Slow and Processive Microtubule Growth In Vitro

We set out to determine the impact of $CPAP_{mini}$ on microtubule dynamics. Strikingly, we found that $CPAP_{mini}$ strongly reduced the rate of microtubule growth (Figures 3E and 3H). This effect could not be explained by tubulin sequestration, because the concentration of $CPAP_{mini}$ in these experiments (75–100 nM) was much lower than that of tubulin (15 μM). Furthermore, $CPAP_{mini}$ dramatically reduced the frequency of catastrophes and promoted rescues, together leading to highly processive microtubule polymerization (Figures 3E, 3I, and 3J). This effect was also observed in the presence of EB3, despite the fact that EB3 itself causes a ~1.5-fold increase in microtubule growth rate and a ~3-fold increase in catastrophe frequency (Figures 3F and 3K–3M). To test whether the artificial dimerization domain of GCN4 in $CPAP_{mini}$ has an influence on microtubule dynamics, we purified a CPAP construct that contains the endogenous coiled coil ($CPAP_{long}$; Figures S2A and S2C). Although $CPAP_{long}$ had a higher propensity for degradation and aggregation, it also bound to microtubule plus ends, very similarly to $CPAP_{mini}$, and had a similar effect on microtubule dynamics: it reduced both the growth rate and the catastrophe frequency, and increased the rescue frequency (Figures S2D–S2G). These data demonstrate that GCN4 links $CPAP_{mini}$ polypeptide chains in a fashion similar to that of the endogenous coiled-coil domain.

Next, we tested the effect of mutations that disrupt either the tubulin-SAC (KR/EE, FF/AA) or the tubulin-LID interaction (ΔLID, FEY/AAA) on the ability of $CPAP_{mini}$ to regulate microtubule plus-end dynamics (Figures 1A and S2A). We found that all four mutants abrogated tip enrichment, as well as the effects on microtubule growth and catastrophes (Figures 3G–3L and S2H). In contrast, all mutants, as well as the dimeric version of MBD alone (ΔPN2-3), were still able to bind to the microtubule lattice and induce rescues to an extent similar to that of wild-type $CPAP_{mini}$ (Figures 3G–3M). This result suggests that the MBD has microtubule-stabilizing properties. To further assess the mechanism underlying the activity of $CPAP_{mini}$, we investigated how its concentration affects microtubule dynamics. As mentioned above, at 75 nM of $CPAP_{mini}$, though not at lower concentrations, both the microtubule growth rate and the catastrophe frequency were strongly reduced (Figures 3H–3L, 4A, and 4B). A 4-fold increase in concentration of $CPAP_{mini}$ had little additional effect on the microtubule growth rate and catastrophe frequency, indicating that the effect of $CPAP_{mini}$ on microtubule elongation in vitro saturates at ~75 nM (Figures 4A and 4B).

We next set out to determine the number of $CPAP_{mini}$ molecules at microtubule plus ends. Single-molecule fluorescence

(H–M) Microtubule plus-end growth rate, catastrophe frequency, and rescue frequency in the presence of rhodamine-tubulin alone or together with 20 nM mCherry-EB3 and 100 nM of the indicated $CPAP_{mini}$ variants. ~100–200 microtubule growth events from two to four independent experiments were analyzed per condition. Error bars represent SEM.

Scale bars in (D–G) represent 2 μm (horizontal) and 60 s (vertical). See also Figure S2 and Table S1.

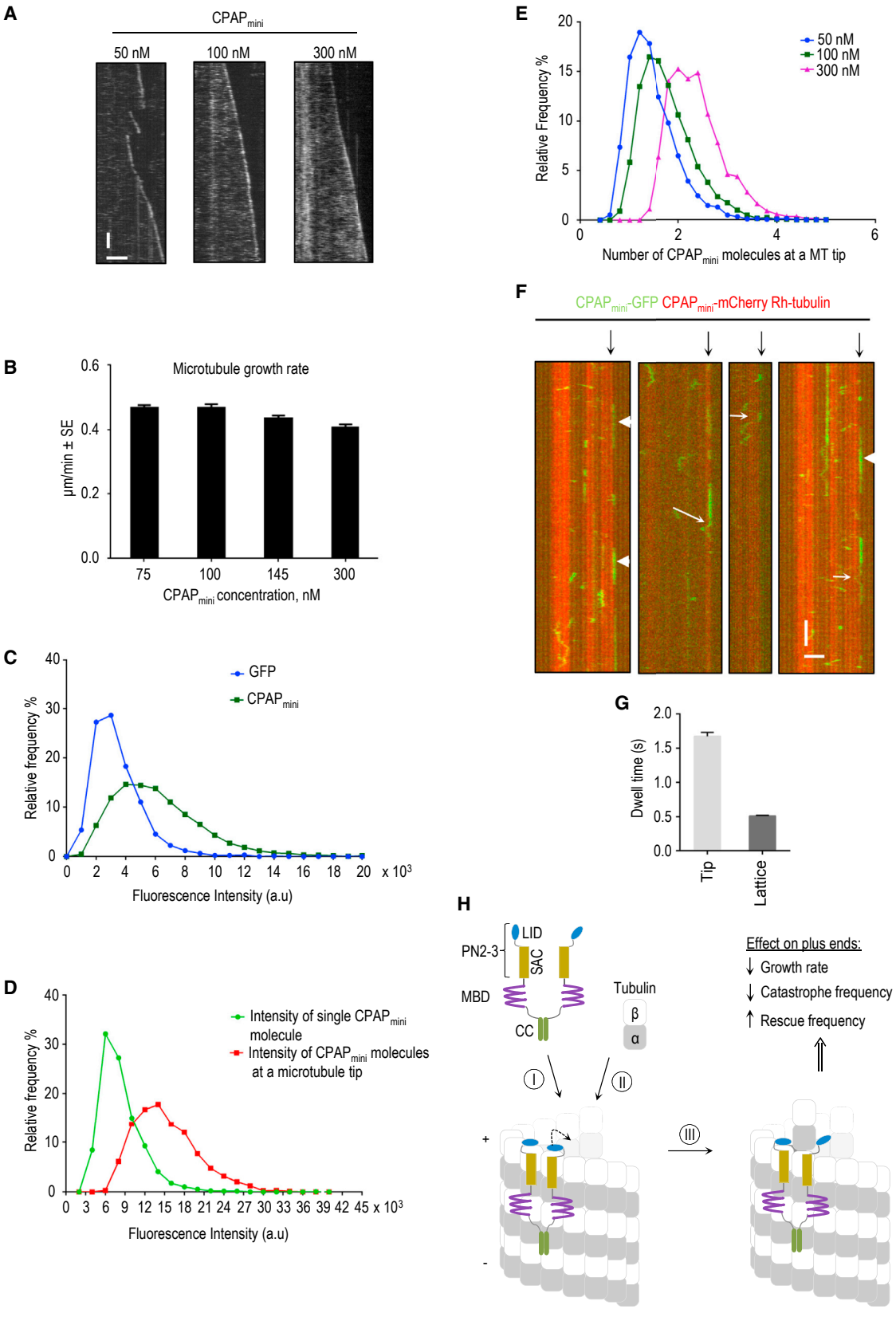

(legend on next page)

intensity analysis of $CPAP_{mini}$ in comparison with GFP confirmed that $CPAP_{mini}$ is a dimer (Figure 4C). To determine the number of $CPAP_{mini}$ molecules at one microtubule tip, we immobilized single $CPAP_{mini}$ molecules on the surface of one flow chamber and performed the in vitro reconstitution assay in the adjacent chamber on the same coverslip. Images of unbleached $CPAP_{mini}$ single molecules were acquired first, after which time-lapse imaging of the in vitro assay with $CPAP_{mini}$ was performed using the same illumination and imaging conditions. We found that approximately two dimers of $CPAP_{mini}$ were present at microtubule tips in the presence of 100 or 300 nM protein, respectively (Figures 4D and 4E). Our tubulin-PN2-3 structural model suggests that $CPAP_{mini}$, which contains two PN2-3 moieties, interacts with microtubule plus ends by binding to terminal β-tubulin subunits (Figure 2D). Our reconstitution data thus indicate that $CPAP_{mini}$ can reach its full activity with respect to microtubule growth inhibition and catastrophe suppression by binding to approximately four protofilaments.

To acquire mechanistic insights into $CPAP_{mini}$ association with the microtubule tip and lattice, we mixed 5 nM $CPAP_{mini}$-GFP (Figure 4F) with 100 nM $CPAP_{mini}$-mCherry. This approach allowed us to observe the behavior of single $CPAP_{mini}$-GFP molecules in conditions whereby the protein inhibits microtubule growth. Rapid imaging of such samples showed that in most cases $CPAP_{mini}$ directly associated with the microtubule plus end, where it remained stationary and then detached. Occasionally, we observed $CPAP_{mini}$ molecules diffusing toward or away from the microtubule tip (Figure 4F). The analysis of binding events of $CPAP_{mini}$ at growing microtubule plus ends yielded an exponential dwell-time distribution with a mean value of ~1.7 s (corrected for photobleaching [Helenius et al., 2006]) (Figures 4G, S3A, and S3B). The dwell time for $CPAP_{mini}$ was longer than those observed previously for EB1, EB3, and CLIP-170 in similar conditions (values ranged between ~0.05 and 0.3 s [Bieling et al., 2008; Montenegro Gouveia et al., 2010]). We also observed binding and unbinding of $CPAP_{mini}$ to the microtubule lattice, with an average dwell time of ~0.5 s (Figures 4G, S3A, and S3B). On the lattice, both stationary and mobile $CPAP_{mini}$ molecules were detected. We noted that a single $CPAP_{mini}$ molecule could switch between the two types of behavior (Figure 4F). Automated single-particle tracking combined with mean squared displacement (MSD) analysis indicated that the mobile $CPAP_{mini}$ molecule population undergoes one-dimensional diffusion, as the increase of the MSD value over time was linear (Figures S3C–S3E) (Qian et al., 1991). The diffusion coefficient of $CPAP_{mini}$ bound to microtubule lattices was 0.03 ± 0.0004 $\mu m^2\ s^{-1}$ (Table S3). This value is three times lower than that for EB3 and similar to the one for the kinesin-13 MCAK, obtained under similar conditions (Montenegro Gouveia et al., 2010).

Taken together, these results demonstrate that $CPAP_{mini}$ localizes to microtubule plus ends mostly through direct binding and remains largely immobile at the microtubule tip until detachment. This behavior, as well as the longer dwell times at the microtubule plus end compared with the lattice, can be explained by the presence of the LID domain, which can attach $CPAP_{mini}$ to the tip of a protofilament. Our data further show that $CPAP_{mini}$ can either diffuse along the lattice or bind to it in a stationary manner. We think that these two types of $CPAP_{mini}$ behavior might be due to the presence of the MBD and SAC domains, which can independently interact with microtubule lattices. Finally, our results demonstrate that $CPAP_{mini}$ suppresses microtubule growth and stabilizes microtubules by inhibiting catastrophes and promoting rescues. In combination with the structural and biophysical data, our reconstitution data suggest that $CPAP_{mini}$ ensures slow processive microtubule growth by capping and stabilizing the plus ends of protofilaments (Figure 4H).

Both the SAC and MBD Domains of CPAP Are Essential for Centriole Assembly

Our in vitro observations raised the possibility that CPAP could contribute to centriole formation in two ways: the MBD could promote centriolar microtubule assembly by stabilizing microtubules, while LID, together with SAC, might limit centriolar microtubule elongation by slowing growth of their plus ends. To test these predictions in the cellular context, we generated cell lines conditionally expressing YFP-tagged CPAP transgenes resistant to RNAi targeting endogenous CPAP (Kitagawa et al., 2011). We analyzed mitotic cells using the centriolar marker Centrin 2 as a readout of successful centriole assembly. Whereas >90% of

Figure 4. Counting of $CPAP_{mini}$ Molecules at Microtubule Plus Ends

(A) Kymographs illustrating growth dynamics of microtubule plus ends in the presence of 20 nM mCherry-EB3 and indicated concentrations of $CPAP_{mini}$. Only the $CPAP_{mini}$ channel is shown. Scale bars represent 2 μm (horizontal) and 60 s (vertical).

(B) Microtubule growth rates at indicated concentrations of $CPAP_{mini}$ in the presence of 20 nM mCherry-EB3. Error bars represent SEM.

(C) Distribution of fluorescence intensities for single molecules of GFP (blue, mean intensity value $3.4 \times 10^3 \pm 1.6 \times 10^3$) and $CPAP_{mini}$ (green, mean intensity value $6.2 \times 10^3 \pm 3.1 \times 10^3$). Mean intensity values are reported as means ± SD.

(D) Distribution of fluorescence intensity values for single immobilized $CPAP_{mini}$ molecules (green, mean intensity value = $8.3 \times 10^3 \pm 3.2 \times 10^3$) compared to $CPAP_{mini}$ (100 nM) molecules at microtubule tips (red, mean intensity value $15.2 \times 10^3 \pm 4.7 \times 10^3$). Mean intensity values are reported as means ± SD.

(E) Distributions of the numbers of $CPAP_{mini}$ molecules on microtubule plus ends at indicated protein concentrations of $CPAP_{mini}$. At 100 nM, a concentration sufficient to strongly suppress microtubule growth, ~2 $CPAP_{mini}$ dimers were bound to microtubule tips (green curve).

(F) Kymographs of dynamic microtubules grown in the presence of 100 nM $CPAP_{mini}$-mCherry, 5 nM $CPAP_{mini}$-GFP, and rhodamine-tubulin, demonstrating $CPAP_{mini}$ single-molecule behavior at the tip and lattice. Plus ends are indicated by black arrows. White arrows point to examples showing both lattice diffusion and tip tracking, while molecules displaying stationary behavior at the microtubule tips are indicated by arrowheads. Scale bars represent 2 μm (horizontal) and 2 s (vertical).

(G) Mean dwell times for $CPAP_{mini}$ on the microtubule lattice (mean time = 0.51 ± 0.01, n = 258) and tip (mean time = 1.67 ± 0.06, n = 755) obtained from the dwell-time distributions; reported means were corrected for photobleaching. Error bars represent the error of fit (see Supplemental Experimental Procedures).

(H) Working model of how $CPAP_{mini}$ ensures slow processive microtubule growth. CPAP recognizes the microtubule plus end via tandemly arranged LID, SAC, and MBD domains (I). This stabilizes the interaction of the terminal tubulin dimers, "caps" the corresponding protofilaments, and stabilizes the microtubule lattice. "Opening" of LID (dashed curved arrow), spontaneously and/or induced by an incoming tubulin dimer (II), enables processive microtubule tip elongation (III).

See also Figure S3 and Table S3.

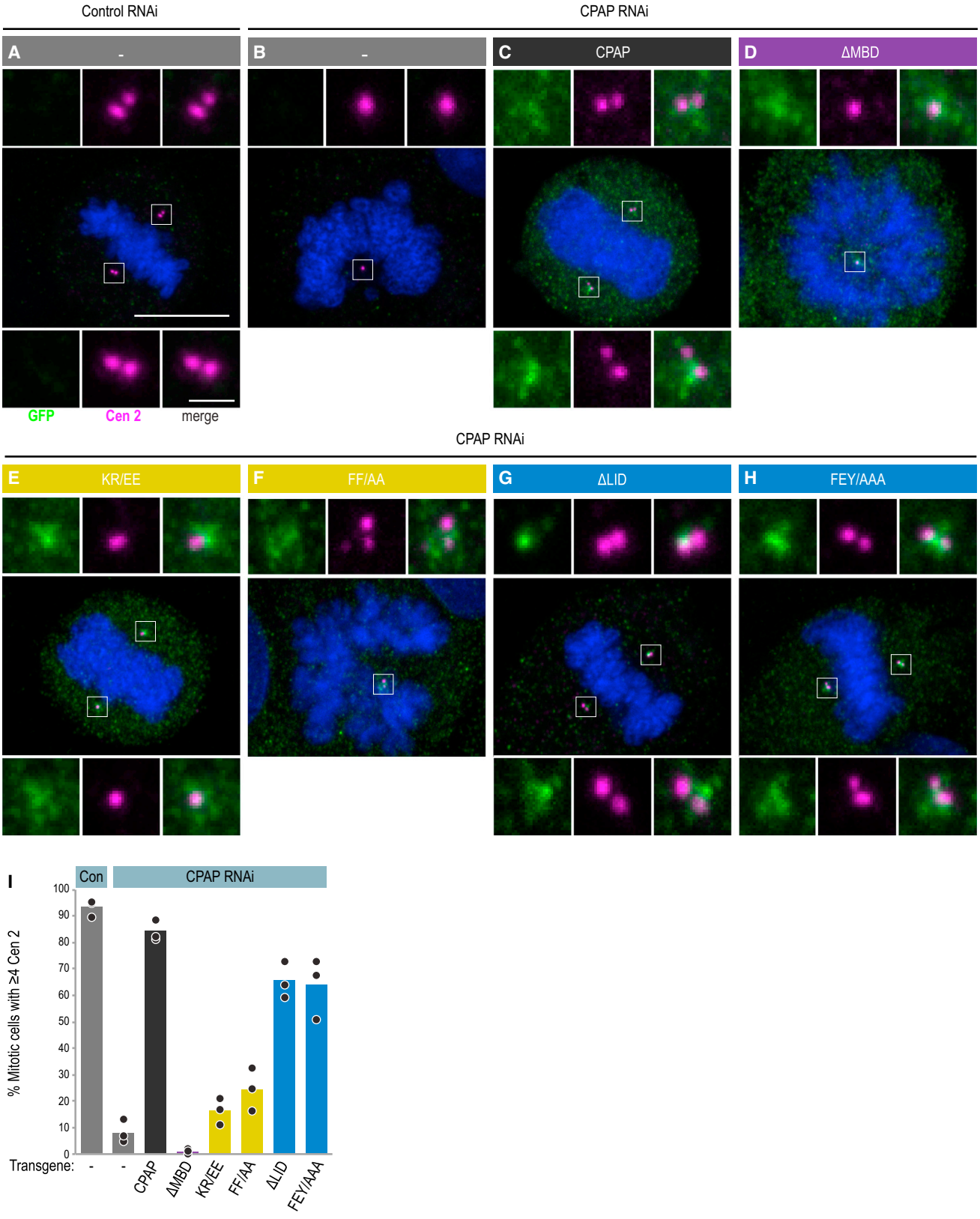

(legend on next page)

control cells contained ≥4 centrioles, this was the case for fewer than 10% of cells depleted of endogenous CPAP (Figures 5A, 5B, 5I, and S4A) (Kohlmaier et al., 2009; Schmidt et al., 2009; Tang et al., 2009). YFP-CPAP rescued this phenotype to a large extent, with >80% of cells having successfully duplicated their centrioles (Figures 5C, 5I, and S4A) (Kohlmaier et al., 2009; Schmidt et al., 2009; Tang et al., 2009). Strikingly, we found that the removal of MBD (ΔMBD) completely abolished centriole assembly, to levels that are even lower than depletion of CPAP alone, likely due to dominant-negative effects following heterodimerization of YFP-CPAP-ΔMBD with any residual endogenous CPAP (Figures 5D, 5I, and S4A). We conclude that the microtubule-stabilizing effect of MBD observed in vitro is essential for centriole biogenesis.

We found also that CPAP constructs lacking the LID domain or with key residues mutated, YFP-CPAP-ΔLID and FEY/AAA, respectively, were able to sustain centriole assembly in ~65% of cells (Figures 5G–5I), indicating that LID contributes to, but is not essential for, this process. In contrast, CPAP function was severely compromised upon mutation of SAC (KR/EE or FF/AA; Figures 5E, 5F, and 5I), in line with previous findings (Hsu et al., 2008; Kitagawa et al., 2011; Tang et al., 2009). Impaired function of all CPAP mutants likely reflects an impact on protein activity, because localization and turnover at the centrosome were unaffected (Figures 5C–5H and S4B). Overall, these results establish that MBD and SAC are critical for centriole assembly, whereas LID appears to play an accessory role in this process.

CPAP Regulates the Length of Centriolar Microtubules in Cells

We further investigated the function of SAC and LID by analyzing cells depleted of endogenous CPAP and overexpressing YFP-CPAP variants, which provided us with an assay system to address the contribution of distinct domains of CPAP to centriole biogenesis. In these conditions, wild-type YFP-CPAP leads to the formation of overly long centrioles that contain not only CPAP but also other centriolar markers such as Centrin 2 along their entire length (Figures 6A and 6D), as reported for cells overexpressing wild-type CPAP in addition to having the endogenous protein (Kohlmaier et al., 2009; Schmidt et al., 2009; Tang et al., 2009). In contrast, we found no overly long centrioles upon YFP-CPAP-ΔMBD overexpression (Figures S4C and S4D), as anticipated from the fact that MBD is essential for centriole assembly. Mutation of SAC (KR/EE or FF/AA) led to a reduction in the proportion of cells with overly long centrioles while deletion of LID had no such effect, again reflecting the respective impact of these variants on the ability of CPAP to sustain regular centriole assembly (Figures 6A, 6D, S4C, and S4D).

Intriguingly, close examination of cells depleted of endogenous CPAP and overexpressing either YFP-CPAP-FF/AA or YFP-CPAP-ΔLID revealed the presence of extended YFP-positive fibers that stemmed from centrosomes, but which did not contain centriolar markers along their length (Figures 6A and 6C). To determine whether such centrosomal fibers originated from centrioles or from the pericentriolar matrix, we conducted immunofluorescence experiments with a marker surrounding the proximal end of parental centrioles (CEP63) and one marking the distal end of all centrioles (Centrin 2). This analysis revealed that ~80% of centrosomal fibers appeared to be continuations of the distal end of regular centrioles or of overly long centrioles, and were thus termed centriole fibers (Figures 6E and 6F). These fibers, lacking Centrin, were often considerably longer than overly long centrioles bearing Centrin (Figure 6H) and were positive for α-tubulin (Figures 6I and 6J), raising the possibility that they correspond to abnormal extensions of centriolar microtubules.

To test this hypothesis, we carried out correlative light and electron microscopy (CLEM; Figures 7 and S5). In line with previous observations (Kohlmaier et al., 2009; Schmidt et al., 2009; Tang et al., 2009), we found that cells overexpressing YFP-CPAP and depleted of endogenous CPAP harbored overly long centrioles, in which microtubules extended from the distal end of the centriole (Figures 7B and 7F; compare with 7A and 7E). Strikingly, cells expressing YFP-CPAP-ΔLID also exhibited microtubule extensions from the distal end of the centriole, which attained several microns in some cases (Figures 7C and 7G). To ensure that such figures represented centriole fibers (i.e., devoid of Centrin) and not overly long centrioles (i.e., bearing Centrin), we carried out further CLEM experiments using tagRFP-Centrin 1 as an additional marker. In agreement with our immunofluorescence analysis, we found that YFP-CPAP-ΔLID centriole fibers were indeed microtubules extending from the distal end of centrioles (Figures 7D and 7H). We conclude that the activities of LID and SAC can prevent aberrant overextension of centriolar microtubules.

DISCUSSION

Our study provides fundamental insights into the mechanisms by which the evolutionarily conserved family of CPAP/SAS-4 proteins regulate the growth of centriolar microtubules, thus contributing to setting organelle size. Whereas the crystal structure of the G box of CPAP, either alone or in complex with a peptide derived from the centriolar protein STIL, has been solved (Zheng et al., 2014; Cottee et al., 2013; Hatzopoulos et al., 2013), high-resolution structural information on the evolutionarily conserved domains interacting with tubulin and microtubules was lacking, precluding full understanding of how CPAP regulates centriole biogenesis. The structural and biophysical data presented here reveal a dual binding mode between tubulin and the LID plus SAC domains of PN2-3, explaining its tubulin-sequestering and

Figure 5. Effect of PN2-3 Mutations on CPAP Cellular Function

(A–H) Mitotic U2OS FlpIn TREX cell lines without transgene (A and B) or expressing the indicated YFP-CPAP variants (C–H), treated with control siRNA (A) or siRNA targeting endogenous CPAP (B–H), stained with antibodies against Centrin 2 (magenta) and GFP (green); DNA in blue. Scale bars in (A) apply to all images and represent 10 μm in main image and 1 μm in insets.

(I) Percentage of cells showing successful centriole duplication (≥4 Centrin 2 foci). Bars show the mean of three experimental repeats; circles indicate the individual values for each experiment. n > 100 cells analyzed for each condition and per experiment. Two-tailed unequal variance t-tests were used to compare each CPAP mutant to the wild type transgene, with the p values < 0.05 for all samples except FEY/AAA (p = 0.0784). Full dataset is shown in Figure S4A.

See also Figure S4 and Table S1.

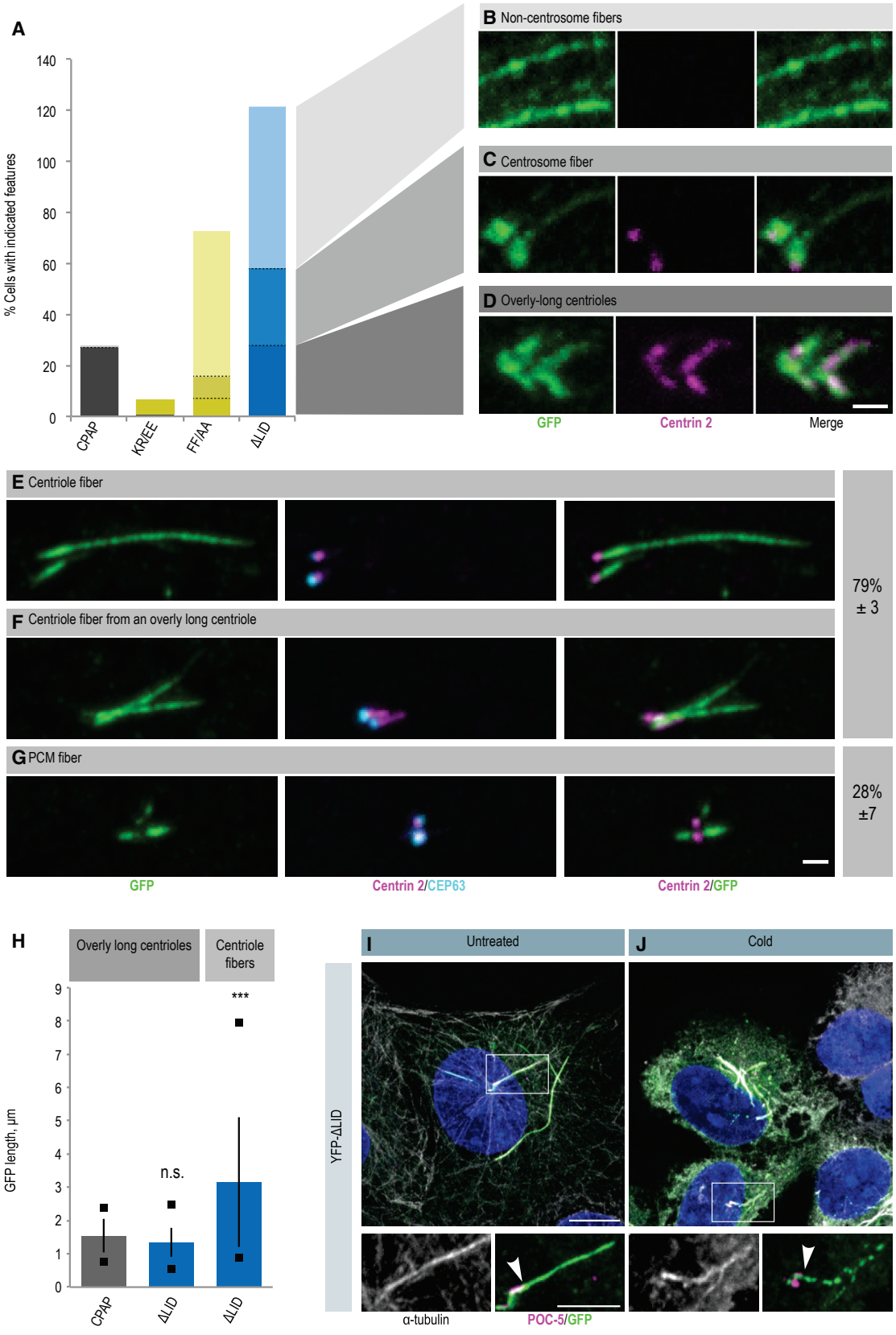

(legend on next page)

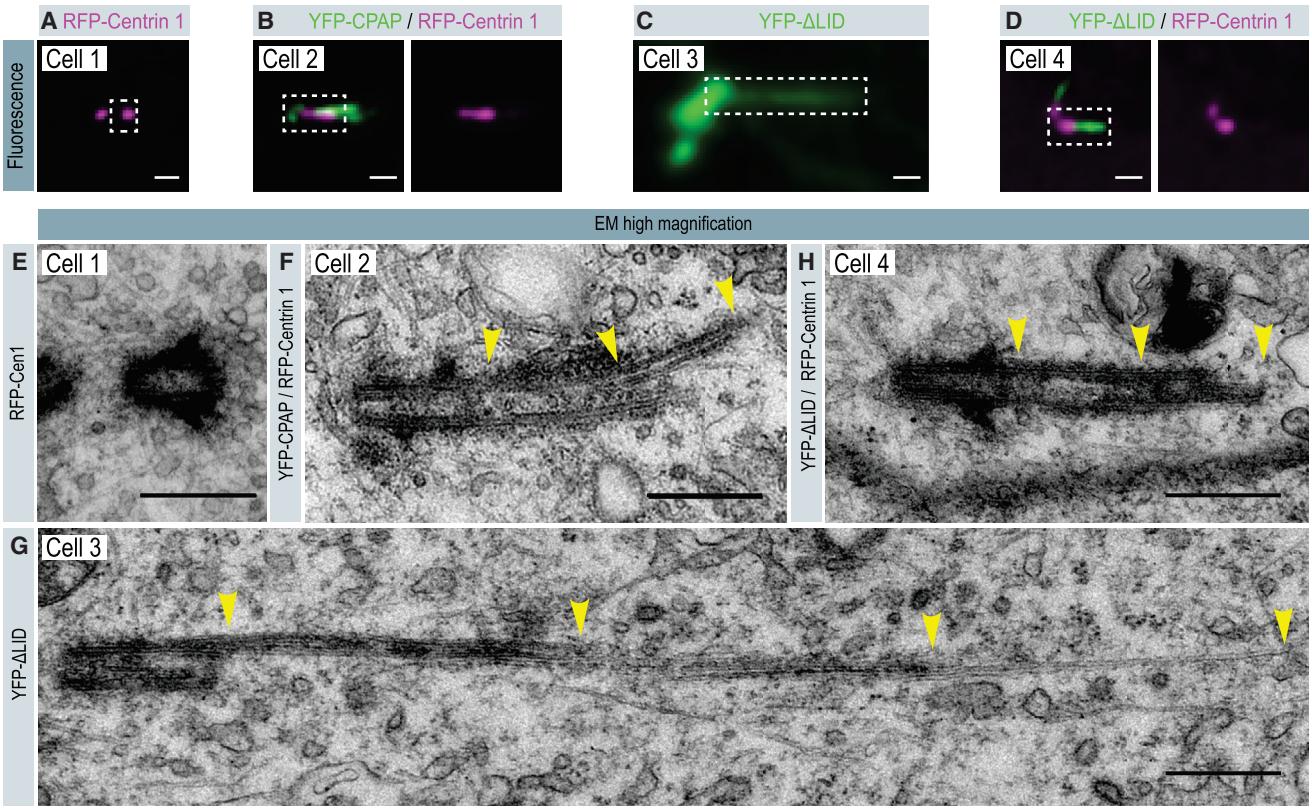

Figure 7. Centriole Fibers Are Centriolar Microtubule Extensions

(A–H) CLEM of cells expressing tagRFP-Centrin 1 (Cell 1; A, E), YFP-CPAP and tagRFP-Centrin 1 (Cell 2; B, F), YFP-ΔLID (Cell 3; C, G), or YFP-ΔLID plus tagRFP-Centrin-1 (Cell 4; D, H), and simultaneously depleted of endogenous CPAP using RNAi (Cells 2–4). (A–D) Fluorescence microscopy images of the region of interest in each cell. Scale bar, 1 μm. (E–H) Corresponding high-magnification electron micrographs of the boxed region in (A–D), showing one 50 nm section from a serial section series. Yellow arrowheads indicate microtubule extensions from the distal ends of centrioles. Scale bars, 500 nm. Ten cells expressing YFP-ΔLID were analyzed, which contained a total of 28 centrioles. Of these, three were centrioles with an apparent normal length and structure, two were overly long centrioles without further microtubule extensions, four exhibited PCM fibers, whereas 19 harbored microtubule extensions from their distal ends (as illustrated in G and H). Of these 19 centrioles, six came from the experiment where cells were also expressing tagRFP-Centrin 1 and could therefore be unambiguously classified as centriole fibers (i.e., without tagRFP-Centrin 1 signal) rather than overly long centrioles.

See also Figures S5 and S6.

microtubule-destabilizing activities (Hsu et al., 2008; Cormier et al., 2009; Hung et al., 2004). The finding that LID binds at the tip of β-tubulin, in combination with the structural model suggesting that PN2-3 can bind the terminal β-tubulin subunits on the outside of a microtubule, strongly suggested that PN2-3 represents an autonomous microtubule plus-end targeting domain in CPAP.

To test whether this is the case, we performed dynamic microtubule reconstitution experiments and indeed found that the sequential arrangement of LID, SAC, and MBD in a dimeric configuration localizes $CPAP_{mini}$ to growing microtubule plus ends. The plus-end localization of $CPAP_{mini}$ is unlikely to depend on co-polymerization with tubulin, because tip localization is observed at $CPAP_{mini}$ concentrations that are several orders of

Figure 6. Fibers Extend from Centrioles upon Expression of CPAP Lacking the LID Domain

(A–D) U2OS cells expressing indicated YFP-CPAP variants and depleted of endogenous CPAP by RNAi, stained with antibodies against Centrin 2 (magenta) and GFP (green). (A) Quantification of the YFP structures illustrated in (B–D) (n > 100 per sample). Note that the total exceeds 100% here and in (E–G) because some cells contain multiple types of structure. Scale bar, 1 μm.

(E–G) Proportion of YFP-CPAP-ΔLID expressing cells with centriole fibers (E and F) or PCM fibers (G). Percentages are the mean of three experiments ± SD; n = 9, 17, and 26 cells, respectively. Scale bar, 1 μm.

(H) Length of overly long centrioles and of centriole fibers in the indicated conditions determined using GFP immunofluorescence. n = 42, 22, and 37 cells, respectively. Bars indicate the mean, squares indicate the minimum and maximum values, and error bars indicate the SD. Student's two-sample two-tailed unequal variance t test comparing ΔLID overly long centrioles and centriole fibers with CPAP-induced overly long centrioles: ***p < 0.001; n.s., not significant.

(I and J) YFP-CPAP-ΔLID cells without (I) or with (J) 1 hr incubation on ice stained with antibodies against α-tubulin (gray), GFP (green), and the distal centriole protein POC5 (magenta). Arrowheads indicate end of centrioles from which emanate fibers, as determined by the POC5 signal. Note that the signal of YFP-CPAP-ΔLID along the centriole fiber becomes sparser following ice-induced microtubule depolymerization. Scale bars represent 10 μm (main image) and 5 μm (inset).

magnitude lower than that of tubulin. Analysis of the behavior of single $CPAP_{mini}$ molecules in our in vitro reconstitution system showed that the majority of $CPAP_{mini}$ molecules bound to microtubule plus ends directly. $CPAP_{mini}$ also displayed one-dimensional diffusion along the microtubule lattice, as described previously for other microtubule-end-interacting proteins (Brouhard et al., 2008; Bieling et al., 2008; Helenius et al., 2006; Montenegro Gouveia et al., 2010); however, diffusion did not seem to be a major contributing factor responsible for the recruitment of $CPAP_{mini}$ to microtubule plus ends. Notably, in the context of a centriole, CPAP is expected to be organized in a precise manner along the inside of the centriole wall where it binds STIL, and is thus very likely not diffusive (Hatzopoulos et al., 2013).

Our reconstitution data revealed that depending on the conditions, microtubule-tip-localized $CPAP_{mini}$ slows down microtubule growth 5- to 8-fold and that only a few $CPAP_{mini}$ molecules suffice to induce this effect. Based on the structural and biophysical results, we propose that the LID and SAC domains of $CPAP_{mini}$ bind terminal β-tubulin subunits exposed at the microtubule plus ends and thereby occlude the binding sites for the incoming tubulin dimers. The ability of PN2-3 to block longitudinal tubulin-tubulin interactions is reminiscent of the tubulin-sequestering protein stathmin and the microtubule plus-end capping ligands DARPin D1, eribulin, and maytansine (Gigant et al., 2000; Pecqueur et al., 2012; Smith et al., 2010; Prota et al., 2014). However, in striking contrast to these microtubule-destabilizing and polymerization-blocking agents, $CPAP_{mini}$ stabilizes microtubules by potently suppressing catastrophes and promoting rescues. The latter property can be attributed to the MBD, which binds strongly to the microtubule lattice and can autonomously induce rescues. The MBD is positively charged, and its binding to negatively charged microtubules likely involves an electrostatic mechanism, similar to that of microtubule lattice-binding regions of cytoplasmic microtubule regulators such as XMAP215/ch-TOG (Brouhard et al., 2008; Widlund et al., 2011). We assume that the MBD of $CPAP_{mini}$ binds along, as well as between, protofilaments to stabilize microtubules.

Based on these considerations, we conclude that this particular mode of binding to microtubule plus ends, due to the combination of LID, SAC, and MBD, can "cap" and stabilize terminal tubulin dimers (Figure 4H). We postulate that in this state, a capped protofilament can only be elongated by an incoming tubulin dimer if the LID domain is released and frees the interaction site needed for establishing longitudinal tubulin-tubulin contacts. The release of LID in turn weakens the $CPAP_{mini}$ microtubule plus-end interaction and either promotes $CPAP_{mini}$ detachment or enables the liberated PN2-3 domain to cap the newly elongated protofilament or a neighboring one. Notably, slowing microtubule growth normally promotes catastrophes by reducing the size of the GTP cap (Walker et al., 1988; Janson et al., 2003). Accordingly, microtubule polymerization suppressors typically act as microtubule depolymerases. However, exceptions to this rule are known, including the kinesin-4 family members Xklp1/KIF4 and KIF21A which, similarly to $CPAP_{mini}$, can suppress both microtubule growth and catastrophes (Bringmann et al., 2004; Bieling et al., 2010; Van der Vaart et al., 2013). The molecular basis of kinesin-4-mediated microtubule growth inhibition is not understood, but is very likely distinct from that of $CPAP_{mini}$, because both Xklp1/KIF4 and KIF21A are molecular motors that can move along microtubules and accumulate at microtubule plus ends due to their processive motility (Bieling et al., 2010; Van der Vaart et al., 2013). In contrast, CPAP presents a unique arrangement of tubulin-binding and microtubule-lattice-binding domains, which together have the potential to recognize, cap, and stabilize microtubule plus ends, a mechanism that to our knowledge has not been previously described for any microtubule regulator.

In cells, centriolar microtubules grow very slowly and processively as judged from the analysis of specimens prepared from different stages of the cell cycle (Kuriyama and Borisy, 1981; Chretien et al., 1997). However, the mechanisms underlying such slow and regulated elongation have remained elusive. Our study reveals that CPAP plays a critical dual role in ensuring that this is the case. First, our data indicate that a pivotal function of CPAP is to stabilize centriolar microtubules via its MBD, which likely explains why this domain is essential for centriole assembly. Second, although the capacity of LID to cap microtubule plus ends is not essential for this stabilization function, and thus for centriole formation, it exerts a negative role by limiting microtubule extension from the distal end of centrioles. The SAC domain, which interacts with the lateral side of tubulin dimers, can contribute to both microtubule stabilization and capping functions, potentially explaining why mutations in SAC affect centriole formation more strongly than those in LID. These considerations can at least partially explain why centrioles overelongate when CPAP dosage is increased (Kohlmaier et al., 2009; Schmidt et al., 2009; Tang et al., 2009); however, additional mechanisms likely control the activity of CPAP domains in cells. Our in vitro data revealed that approximately two $CPAP_{mini}$ dimers are sufficient to limit the growth rate of a single microtubule, suggesting that CPAP works at substoichiometric levels. In the context of the centriolar microtubule wall, we expect approximately two CPAP dimers to be able to access the microtubule tips of each triplet from the luminal side of the centriole (Figure S6) (Hatzopoulos et al., 2013; Sonnen et al., 2012; Tang et al., 2011).

Overall, our results reveal that CPAP is a highly specialized microtubule plus-end regulator that acts as a molecular cap to ensure slow and processive growth of centriolar microtubules. Given that endogenous CPAP is present primarily in the proximal region of mature centrioles (Kohlmaier et al., 2009; Schmidt et al., 2009; Tang et al., 2009), we propose that CPAP activity is most critical during the early stages of centriole elongation. Upon overexpression of the wild-type protein, excess CPAP molecules localize along the entire length of centrioles and could cause overelongation of centriolar microtubules due to the microtubule stabilization activity of ectopic CPAP. Furthermore, we speculate that upon overexpression of a mutant protein lacking LID-domain function, overelongation of centriolar microtubules is exacerbated due to the lack of capping function (Figure S6).

We note that microtubule growth rates obtained in vitro upon $CPAP_{mini}$ addition are still some three orders of magnitude faster than those estimated for centriolar microtubules in cells (Kuriyama and Borisy, 1981; Chretien et al., 1997). Regions of CPAP outside of the microtubule- and tubulin-binding domains,

including the G box, that may organize CPAP molecules along the entire length of the microtubule wall in a precise manner (Hatzopoulos et al., 2013), as well as post-translational modifications, could be important to further bolster CPAP activity; these features are not recapitulated by the $CPAP_{mini}$ and $CPAP_{long}$ constructs used in our study. In addition, other centriolar proteins have been implicated in controlling centriole length, including the CPAP-interacting proteins CEP120, CEP135, and Centrobin (Gudi et al., 2011; Lin et al., 2013a, 2013b). It will be of prime interest to assess on a mechanistic level how these proteins cooperate to impact on CPAP function or otherwise contribute to regulate organelle size.

EXPERIMENTAL PROCEDURES

Protein/Peptide Preparation and Isothermal Titration Calorimetry

Standard protein production in bacteria and peptide synthesis is described in Supplemental Experimental Procedures. ITC experiments were performed at 25°C using an ITC200 system (Microcal). Proteins were buffer-exchanged to BRB80 (80 mM PIPES-KOH [pH 6.8] supplemented with 1 mM $MgCl_2$ and 1 mM EGTA) supplemented with 0.5 mM tris(2-carboxyethyl)phosphine. 0.1–0.4 mM PN2-3 variants in the syringe were injected stepwise into 10–20 μM tubulin solutions in the cell. The resulting heats were integrated and fitted in Origin (OriginLab) using the standard "one set of sites" model provided by the software package.

Structure Determination

Structure solution by X-ray crystallography is described in full in the Supplemental Experimental Procedures. In brief, equimolar amounts of D1, PN2-3, and subtilisin-treated tubulin were mixed and the PN2-3-tubulin-D1 complex was concentrated to ~20 mg/ml. PN2-3-tubulin-D1 samples were complemented with 0.2 mM GDP, 1 mM colchicine, and 5 mM DTT before setting up sitting-drop vapor diffusion crystallization trials. Crystals were obtained in a condition containing 20% polyethylene glycol (PEG) 550 monomethyl ether and 0.1 M 2-(N-morpholino)ethanesulfonic acid (pH 6.5). X-Ray diffraction data were collected at 100 K at beamline X06DA at the Swiss Light Source. The PN2-3-tubulin-D1 structure was solved by molecular replacement using the αβ-tubulin-D1 complex structure as a search model (PDB: 4DRX). Data collection and refinement statistics are given in Table S2.

In Vitro Reconstitution Assays

Protein purification for in vitro reconstitution assays is described in full in Supplemental Experimental Procedures. Reconstitution of microtubule growth dynamics in vitro was performed as described previously (Montenegro Gouveia et al., 2010). In brief, flow chambers were functionalized by sequential incubation with 0.2 mg/ml PLL-PEG-biotin (Susos) and 1 mg/ml NeutrAvidin (Invitrogen) in MRB80 buffer (80 mM piperazine-N,N′-bis(2-ethanesulfonic acid) [pH 6.8] supplemented with 4 mM $MgCl_2$ and 1 mM EGTA). GMPCPP-microtubule seeds were attached to coverslips through biotin-NeutrAvidin interactions. The reaction mix with or without $CPAP_{mini}$ proteins (MRB80 buffer supplemented with 15 μM tubulin, 0.5 μM rhodamine-tubulin, 50 mM KCl, 1 mM guanosine triphosphate, 0.2 mg/ml κ-casein, 0.1% methylcellulose, and oxygen scavenger mix [50 mM glucose, 400 μg/ml glucose oxidase, 200 μg/ml catalase, and 4 mM DTT]) was added to the flow chamber. Flow chambers were sealed and dynamic microtubules were imaged immediately at 30°C using TIRF microscopy. Intensity analysis for $CPAP_{mini}$ along microtubules, single-molecule fluorescence intensity analysis of $CPAP_{mini}$, $CPAP_{mini}$ molecule counting at microtubule tips, analysis of microtubule plus-end dynamics, and statistical analysis procedures are all described in full in Supplemental Experimental Procedures.

Immunofluorescence, Antibodies, and Microscopy

Cells were grown on glass coverslips and fixed in methanol for 7 min at −20°C. Cold treatment was carried out by incubating cells in ice-cold PBS, on ice, for 1 hr before fixation. Cells were permeabilized using 0.2% Triton X-100, washed in PBS and 0.01% Triton X-100, and blocked for 1 hr in PBS, 1% BSA, and 2% fetal calf serum. All antibodies were diluted in the blocking solution and incubated for either 1 hr at room temperature or ~12 hr at 4°C. Primary antibodies were mouse anti-α-tubulin (DM1a, Sigma), mouse "20H5" anti-centrin-2 (a gift from J. Salisbury), rabbit anti-hPOC5 (Azimzadeh et al., 2009; a gift from M. Bornens), rabbit anti-CEP63 (Millipore 06-1292), goat anti-GFP (Abcam ab6673), and rabbit anti-GFP (a gift from V. Simanis). Secondary antibodies were goat anti-rabbit Alexa Fluor 488, goat anti-mouse Alexa Fluor 568, donkey anti-goat Alexa Fluor 488, donkey anti-mouse Alexa Fluor 568, and donkey anti-rabbit Alexa Fluor 647 (Invitrogen). All primary antibodies were diluted 1,000-fold, except Centrin 2 (2000×) and anti-α-tubulin (5000×). All secondary antibodies were diluted 1,000-fold. Samples were washed three times between, and after, antibody incubations and incubated with 1 μg/ml Hoechst in PBS prior to mounting in PBS, 90% glycerol, and 4% N-propyl gallate.

Confocal imaging was carried out using a Zeiss LSM 700 microscope with a Plan-Apochromat 63× oil-immersion objective, NA 1.40. Z sections were imaged at an interval of ~0.2 μm. All images shown are maximum-intensity projections and were processed using Fiji (Schindelin et al., 2012), maintaining relative intensities within a series.

Correlative Light and Electron Microscopy

CLEM is described in full in Supplemental Experimental Procedures. In brief, endogenous CPAP was depleted by RNAi for 72 hr, simultaneous with induction of the transgene. For dual marker experiments, cells were transfected with a tagRFP-Centrin 1 expression vector 16 hr prior to fixation. Cells were fixed, then washed thoroughly with 0.1 M cacodylate buffer (pH 7.4), and imaged by light microscopy. Immediately afterward, samples were post-fixed for 40 min in 1.0% osmium tetroxide, then 30 min in 1.0% uranyl acetate in water, before being dehydrated through increasing concentrations of alcohol and then embedded in Durcupan ACM resin (Fluka). The coverslips were then placed face down on a glass slide coated with mold-releasing agent (Glorex), with approximately 1 mm of resin separating the two. These regions were mounted on blank resin blocks with acrylic glue and trimmed with glass knives to form a block ready for serial sectioning. Series of between 150 and 300 thin sections (50 nm thickness) were cut with a diamond knife mounted on an ultramicrotome (Leica UC7). These sections were contrasted with lead citrate and uranyl acetate and images taken using an FEI Spirit transmission electron microscope equipped with an Eagle CCD camera.

ACCESSION NUMBERS

Coordinates have been deposited in the PDB under accession number PDB: 5ITZ (D1-tubulin-PN2-3).

SUPPLEMENTAL INFORMATION

Supplemental Information includes Supplemental Experimental Procedures, six figures, and three tables and can be found with this article online at http://dx.doi.org/10.1016/j.devcel.2016.04.024.

AUTHOR CONTRIBUTIONS

A.S., A. Aher, N.J.D., E.A.K., M.C., R.A.K., A. Akhmanova, P.G., and M.O.S. designed the experiments. A.S., A. Aher, N.J.D., D.F., E.A.K., R.J., I.G., and M.C. conducted the experiments. A.S., A. Aher, N.J.D., A. Akhmanova, P.G., and M.O.S. wrote the manuscript with input from all the authors.

ACKNOWLEDGMENTS

X-ray data were collected at beamline X06DA of the Swiss Light Source (Paul Scherrer Institut, Villigen, Switzerland). Eribulin was a kind gift from Eisai Co. We are grateful to Graham Knott, head of the Bio-EM Facility in the School of Life Sciences at EPFL, for help in setting up CLEM, and to Christian Arquint and Erich Nigg (Basel, Switzerland) for their gift of the U2OS FlpIn TREX cell line. We thank Marileen Dogterom, Virginie Hachet, and John Vakonakis for useful comments on the manuscript. This work was supported by an EMBO Long Term Fellowship (to A.S.), as well as by grants from the Swiss National

Science Foundation (310030B_138659 and 31003A_166608 to M.O.S.) and the European Research Council (AdG 340227 to P.G. and Synergy grant 609822 to A.A.).

Received: January 19, 2016
Revised: April 4, 2016
Accepted: April 26, 2016
Published: May 23, 2016

REFERENCES

Alday, P.H., and Correia, J.J. (2009). Macromolecular interaction of halichondrin B analogues eribulin (E7389) and ER-076349 with tubulin by analytical ultracentrifugation. Biochemistry *48*, 7927–7938.

Azimzadeh, J., and Marshall, W.F. (2010). Building the centriole. Curr. Biol. *20*, R816–R825.

Azimzadeh, J., Hergert, P., Delouvee, A., Euteneuer, U., Formstecher, E., Khodjakov, A., and Bornens, M. (2009). hPOC5 is a centrin-binding protein required for assembly of full-length centrioles. J. Cell Biol. *185*, 101–114.

Bieling, P., Laan, L., Schek, H., Munteanu, E.L., Sandblad, L., Dogterom, M., Brunner, D., and Surrey, T. (2007). Reconstitution of a microtubule plus-end tracking system in vitro. Nature *450*, 1100–1105.

Bieling, P., Kandels-Lewis, S., Telley, I.A., van, D.J., Janke, C., and Surrey, T. (2008). CLIP-170 tracks growing microtubule ends by dynamically recognizing composite EB1/tubulin-binding sites. J. Cell Biol. *183*, 1223–1233.

Bieling, P., Telley, I.A., and Surrey, T. (2010). A minimal midzone protein module controls formation and length of antiparallel microtubule overlaps. Cell *142*, 420–432.

Bond, J., Roberts, E., Springell, K., Lizarraga, S.B., Scott, S., Higgins, J., Hampshire, D.J., Morrison, E.E., Leal, G.F., Silva, E.O., et al. (2005). A centrosomal mechanism involving CDK5RAP2 and CENPJ controls brain size. Nat. Genet. *37*, 353–355.

Bornens, M. (2012). The centrosome in cells and organisms. Science *335*, 422–426.

Bringmann, H., Skiniotis, G., Spilker, A., Kandels-Lewis, S., Vernos, I., and Surrey, T. (2004). A kinesin-like motor inhibits microtubule dynamic instability. Science *303*, 1519–1522.

Brouhard, G.J., Stear, J.H., Noetzel, T.L., Al-Bassam, J., Kinoshita, K., Harrison, S.C., Howard, J., and Hyman, A.A. (2008). XMAP215 is a processive microtubule polymerase. Cell *132*, 79–88.

Chretien, D., Buendia, B., Fuller, S.D., and Karsenti, E. (1997). Reconstruction of the centrosome cycle from cryoelectron micrographs. J. Struct. Biol. *120*, 117–133.

Cormier, A., Clement, M.J., Knossow, M., Lachkar, S., Savarin, P., Toma, F., Sobel, A., Gigant, B., and Curmi, P.A. (2009). The PN2-3 domain of centrosomal P4.1-associated protein implements a novel mechanism for tubulin sequestration. J. Biol. Chem. *284*, 6909–6917.

Cottee, M.A., Muschalik, N., Wong, Y.L., Johnson, C.M., Johnson, S., Andreeva, A., Oegema, K., Lea, S.M., Raff, J.W., and van, B.M. (2013). Crystal structures of the CPAP/STIL complex reveal its role in centriole assembly and human microcephaly. Elife *2*, e01071.

Gigant, B., Curmi, P.A., Martin-Barbey, C., Charbaut, E., Lachkar, S., Lebeau, L., Siavoshian, S., Sobel, A., and Knossow, M. (2000). The 4 A X-ray structure of a tubulin:stathmin-like domain complex. Cell *102*, 809–816.

Gigant, B., Wang, C., Ravelli, R.B., Roussi, F., Steinmetz, M.O., Curmi, P.A., Sobel, A., and Knossow, M. (2005). Structural basis for the regulation of tubulin by vinblastine. Nature *435*, 519–522.

Gönczy, P. (2012). Towards a molecular architecture of centriole assembly. Nat. Rev. Mol. Cell Biol. *13*, 425–435.

Gönczy, P. (2015). Centrosomes and cancer: revisiting a long-standing relationship. Nat. Rev. Cancer *15*, 639–652.

Gopalakrishnan, J., Chim, Y.C., Ha, A., Basiri, M.L., Lerit, D.A., Rusan, N.M., and Avidor-Reiss, T. (2012). Tubulin nucleotide status controls Sas-4-dependent pericentriolar material recruitment. Nat. Cell Biol. *14*, 865–873.

Gudi, R., Zou, C., Li, J., and Gao, Q. (2011). Centrobin-tubulin interaction is required for centriole elongation and stability. J. Cell Biol. *193*, 711–725.

Hatzopoulos, G.N., Erat, M.C., Cutts, E., Rogala, K.B., Slater, L.M., Stansfeld, P.J., and Vakonakis, I. (2013). Structural analysis of the G-box domain of the microcephaly protein CPAP suggests a role in centriole architecture. Structure *21*, 2069–2077.

Helenius, J., Brouhard, G., Kalaidzidis, Y., Diez, S., and Howard, J. (2006). The depolymerizing kinesin MCAK uses lattice diffusion to rapidly target microtubule ends. Nature *441*, 115–119.

Hsu, W.B., Hung, L.Y., Tang, C.J., Su, C.L., Chang, Y., and Tang, T.K. (2008). Functional characterization of the microtubule-binding and -destabilizing domains of CPAP and d-SAS-4. Exp. Cell Res. *314*, 2591–2602.

Hung, L.Y., Chen, H.L., Chang, C.W., Li, B.R., and Tang, T.K. (2004). Identification of a novel microtubule-destabilizing motif in CPAP that binds to tubulin heterodimers and inhibits microtubule assembly. Mol. Biol. Cell *15*, 2697–2706.

Jana, S.C., Marteil, G., and Bettencourt-Dias, M. (2014). Mapping molecules to structure: unveiling secrets of centriole and cilia assembly with near-atomic resolution. Curr. Opin. Cell Biol. *26*, 96–106.

Janson, M.E., de Dood, M.E., and Dogterom, M. (2003). Dynamic instability of microtubules is regulated by force. J. Cell Biol. *161*, 1029–1034.

Jiang, K., Hua, S., Mohan, R., Grigoriev, I., Yau, K.W., Liu, Q., Katrukha, E.A., Altelaar, A.F., Heck, A.J., Hoogenraad, C.C., et al. (2014). Microtubule minus-end stabilization by polymerization-driven CAMSAP deposition. Dev. Cell *28*, 295–309.

Kinoshita, K., Arnal, I., Desai, A., Drechsel, D.N., and Hyman, A.A. (2001). Reconstitution of physiological microtubule dynamics using purified components. Science *294*, 1340–1343.

Kirkham, M., Muller-Reichert, T., Oegema, K., Grill, S., and Hyman, A.A. (2003). SAS-4 is a *C. elegans* centriolar protein that controls centrosome size. Cell *112*, 575–587.

Kitagawa, D., Kohlmaier, G., Keller, D., Strnad, P., Balestra, F.R., Fluckiger, I., and Gönczy, P. (2011). Spindle positioning in human cells relies on proper centriole formation and on the microcephaly proteins CPAP and STIL. J. Cell Sci. *124*, 3884–3893.

Kohlmaier, G., Loncarek, J., Meng, X., McEwen, B.F., Mogensen, M.M., Spektor, A., Dynlacht, B.D., Khodjakov, A., and Gönczy, P. (2009). Overly long centrioles and defective cell division upon excess of the SAS-4-related protein CPAP. Curr. Biol. *19*, 1012–1018.

Kuriyama, R., and Borisy, G.G. (1981). Centriole cycle in Chinese hamster ovary cells as determined by whole-mount electron microscopy. J. Cell Biol. *91*, 814–821.

Leidel, S., and Gönczy, P. (2003). SAS-4 is essential for centrosome duplication in *C elegans* and is recruited to daughter centrioles once per cell cycle. Dev. Cell *4*, 431–439.

Lin, Y.C., Chang, C.W., Hsu, W.B., Tang, C.J., Lin, Y.N., Chou, E.J., Wu, C.T., and Tang, T.K. (2013a). Human microcephaly protein CEP135 binds to hSAS-6 and CPAP, and is required for centriole assembly. EMBO J. *32*, 1141–1154.

Lin, Y.N., Wu, C.T., Lin, Y.C., Hsu, W.B., Tang, C.J., Chang, C.W., and Tang, T.K. (2013b). CEP120 interacts with CPAP and positively regulates centriole elongation. J. Cell Biol. *202*, 211–219.

Montenegro Gouveia, S., Leslie, K., Kapitein, L.C., Buey, R.M., Grigoriev, I., Wagenbach, M., Smal, I., Meijering, E., Hoogenraad, C.C., Wordeman, L., et al. (2010). In vitro reconstitution of the functional interplay between MCAK and EB3 at microtubule plus ends. Curr. Biol. *20*, 1717–1722.

Nigg, E.A., and Raff, J.W. (2009). Centrioles, centrosomes, and cilia in health and disease. Cell *139*, 663–678.

O'Shea, E.K., Klemm, J.D., Kim, P.S., and Alber, T. (1991). X-ray structure of the GCN4 leucine zipper, a two-stranded, parallel coiled coil. Science *254*, 539–544.

Pecqueur, L., Duellberg, C., Dreier, B., Jiang, Q., Wang, C., Pluckthun, A., Surrey, T., Gigant, B., and Knossow, M. (2012). A designed ankyrin repeat protein selected to bind to tubulin caps the microtubule plus end. Proc. Natl. Acad. Sci. USA *109*, 12011–12016.

Prota, A.E., Bargsten, K., Diaz, J.F., Marsh, M., Cuevas, C., Liniger, M., Neuhaus, C., Andreu, J.M., Altmann, K.H., and Steinmetz, M.O. (2014). A new tubulin-binding site and pharmacophore for microtubule-destabilizing anticancer drugs. Proc. Natl. Acad. Sci. USA *111*, 13817–13821.

Qian, H., Sheetz, M.P., and Elson, E.L. (1991). Single particle tracking. Analysis of diffusion and flow in two-dimensional systems. Biophys. J. *60*, 910–921.

Schindelin, J., Arganda-Carreras, I., Frise, E., Kaynig, V., Longair, M., Pietzsch, T., Preibisch, S., Rueden, C., Saalfeld, S., Schmid, B., et al. (2012). Fiji: an open-source platform for biological-image analysis. Nat. Methods *9*, 676–682.

Schmidt, T.I., Kleylein-Sohn, J., Westendorf, J., Le, C.M., Lavoie, S.B., Stierhof, Y.D., and Nigg, E.A. (2009). Control of centriole length by CPAP and CP110. Curr. Biol. *19*, 1005–1011.

Smith, J.A., Wilson, L., Azarenko, O., Zhu, X., Lewis, B.M., Littlefield, B.A., and Jordan, M.A. (2010). Eribulin binds at microtubule ends to a single site on tubulin to suppress dynamic instability. Biochemistry *49*, 1331–1337.

Sonnen, K.F., Schermelleh, L., Leonhardt, H., and Nigg, E.A. (2012). 3D-structured illumination microscopy provides novel insight into architecture of human centrosomes. Biol. Open *1*, 965–976.

Tang, C.J., Fu, R.H., Wu, K.S., Hsu, W.B., and Tang, T.K. (2009). CPAP is a cell-cycle regulated protein that controls centriole length. Nat. Cell Biol. *11*, 825–831.

Tang, C.J., Lin, S.Y., Hsu, W.B., Lin, Y.N., Wu, C.T., Lin, Y.C., Chang, C.W., Wu, K.S., and Tang, T.K. (2011). The human microcephaly protein STIL interacts with CPAP and is required for procentriole formation. EMBO J. *30*, 4790–4804.

Van der Vaart, B., van Riel, W.E., Doodhi, H., Kevenaar, J.T., Katrukha, E.A., Gumy, L., Bouchet, B.P., Grigoriev, I., Spangler, S.A., Yu, K.L., et al. (2013). CFEOM1-associated kinesin KIF21A is a cortical microtubule growth inhibitor. Dev. Cell *27*, 145–160.

Walker, R.A., O'Brien, E.T., Pryer, N.K., Soboeiro, M.F., Voter, W.A., Erickson, H.P., and Salmon, E.D. (1988). Dynamic instability of individual microtubules analyzed by video light microscopy: rate constants and transition frequencies. J. Cell Biol. *107*, 1437–1448.

Widlund, P.O., Stear, J.H., Pozniakovsky, A., Zanic, M., Reber, S., Brouhard, G.J., Hyman, A.A., and Howard, J. (2011). XMAP215 polymerase activity is built by combining multiple tubulin-binding TOG domains and a basic lattice-binding region. Proc. Natl. Acad. Sci. USA *108*, 2741–2746.

Zhang, R., Alushin, G.M., Brown, A., and Nogales, E. (2015). Mechanistic origin of microtubule dynamic instability and its modulation by EB proteins. Cell *162*, 849–859.

Zhao, L., Jin, C., Chu, Y., Varghese, C., Hua, S., Yan, F., Miao, Y., Liu, J., Mann, D., Ding, X., et al. (2010). Dimerization of CPAP orchestrates centrosome cohesion plasticity. J. Biol. Chem. *285*, 2488–2497.

Zheng, X., Gooi, L.M., Wason, A., Gabriel, E., Mehrjardi, N.Z., Yang, Q., Zhang, X., Debec, A., Basiri, M.L., Avidor-Reiss, T., et al. (2014). Conserved TCP domain of Sas-4/CPAP is essential for pericentriolar material tethering during centrosome biogenesis. Proc. Natl. Acad. Sci. USA *111*, E354–E363.

Developmental Cell, Volume *37*

Supplemental Information

Centriolar CPAP/SAS-4 Imparts Slow Processive Microtubule Growth

Ashwani Sharma, Amol Aher, Nicola J. Dynes, Daniel Frey, Eugene A. Katrukha, Rolf Jaussi, Ilya Grigoriev, Marie Croisier, Richard A. Kammerer, Anna Akhmanova, Pierre Gönczy, and Michel O. Steinmetz

Figure S1

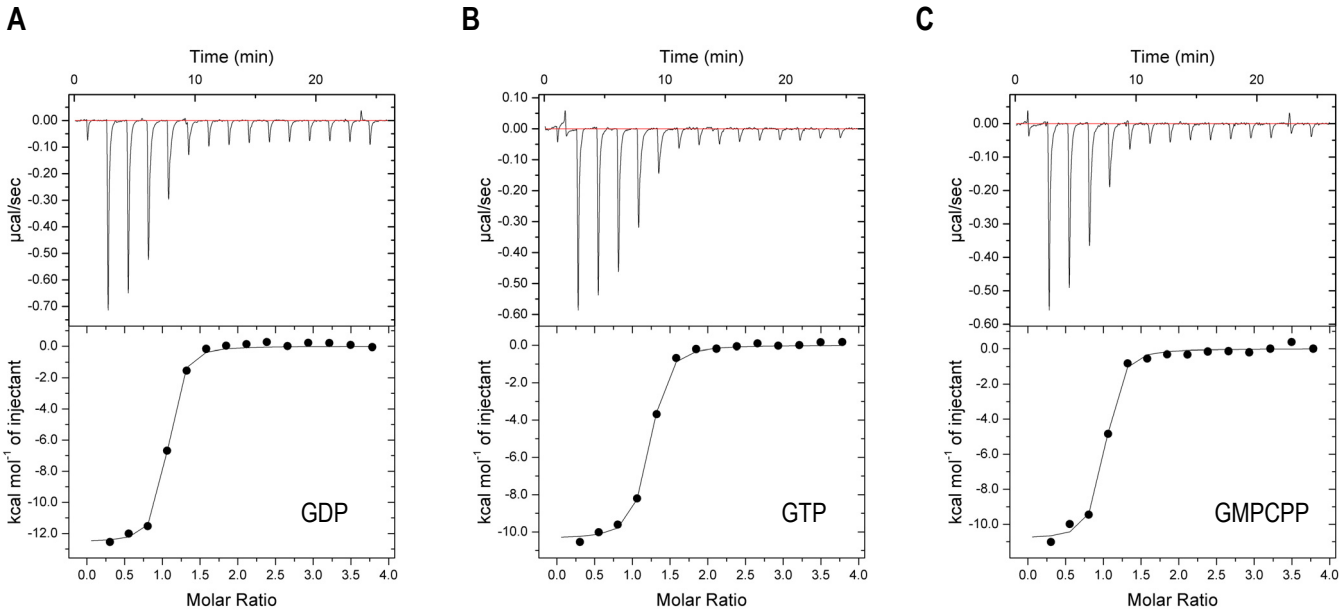
A
B
C
Time (min)
µcal/sec
kcal mol-1 of injectant
Molar Ratio
GDP
GTP
GMPCPP

Figure S1, related to Figure 2. Effect of nucleotide state of tubulin on the interaction with PN2-3s.

(A-C) ITC analysis of the interaction between PN2-3s and tubulin. Experiments were performed by step wise titration of 200 μM PN2-3s in the syringe into 10 μM tubulin in the cell. Upper panels display raw data; lower panels show the integrated heat changes and associated curve fits. The derived Kd values are as follows: 75 ± 12 nM for GDP-tubulin (A), 99 ± 13 nM for GTP-tubulin (B), and 97 ± 20 nM for GMPCPP-tubulin (C).

Figure S2

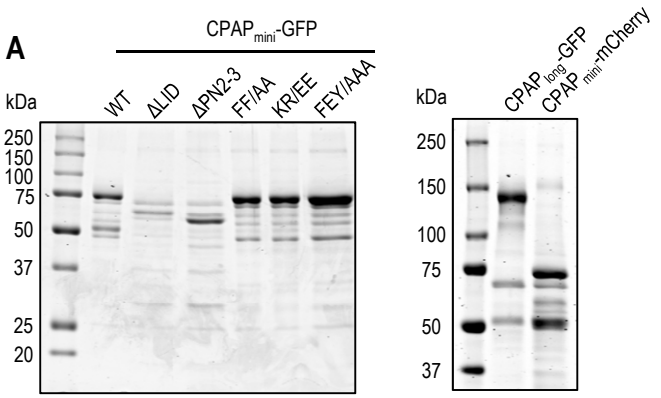
A
CPAP$_{mini}$-GFP
kDa
WT
ΔLID
ΔPN2-3
FF/AA
KR/EE
FEY/AAA
250
150
100
75
50
37
25
20
kDa
CPAP$_{long}$-GFP
CPAP$_{mini}$-mCherry
250
150
100
75
50
37

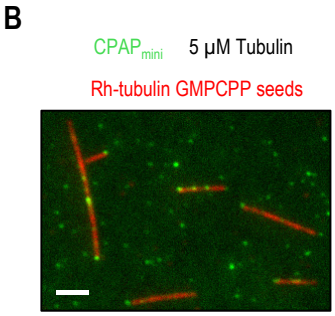
B
CPAP$_{mini}$ 5 µM Tubulin
Rh-tubulin GMPCPP seeds

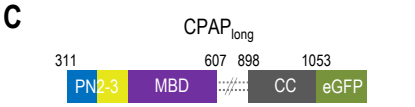
C
CPAP$_{long}$
311
607
898
1053
PN2-3
MBD
CC
eGFP

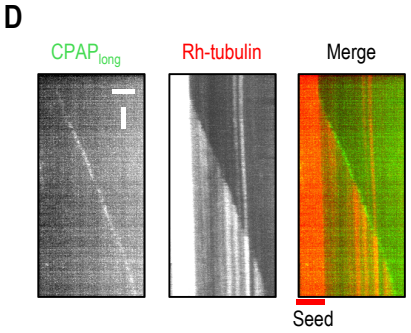
D
CPAP$_{long}$
Rh-tubulin
Merge
Seed

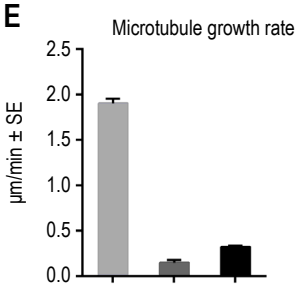
E
Microtubule growth rate
µm/min ± SE
2.5
2.0
1.5
1.0
0.5
0.0

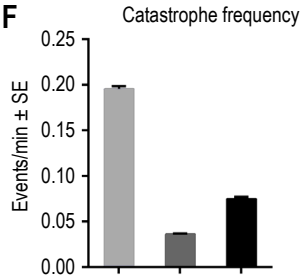
F
Catastrophe frequency
Events/min ± SE
0.25
0.20
0.15
0.10
0.05
0.00

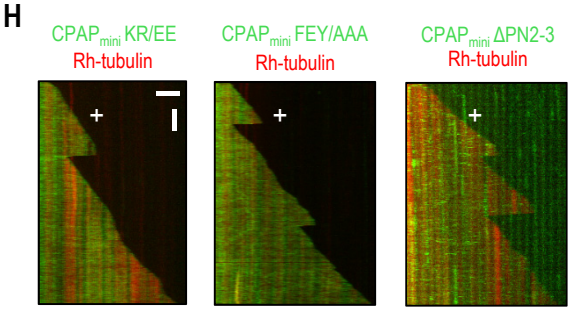
H
CPAP$_{mini}$ KR/EE
Rh-tubulin
CPAP$_{mini}$ FEY/AAA
Rh-tubulin
CPAP$_{mini}$ ΔPN2-3
Rh-tubulin

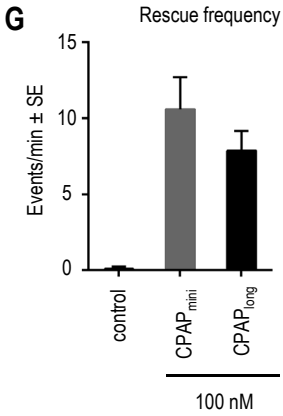
G
Rescue frequency
Events/min ± SE
15
10
5
0
control
CPAP$_{mini}$
CPAP$_{long}$
100 nM

Figure S2, related to Figure 3. Characterization of the effect of $CPAP_{mini}$ on microtubule dynamics in vitro.

(A) Coomassie blue stained gel with $CPAP_{long}$, $CPAP_{mini}$ and its mutants purified from HEK293T cells.

(B) Localization of $CPAP_{mini}$ (green) on rhodamine-labelled GMPCPP stabilized microtubules (red) in the presence of 5 μM tubulin. Although no microtubule growth is observed in these conditions, $CPAP_{mini}$ preferentially binds to one microtubule end, indicating that its plus-end localization does not depend on microtubule polymerization.

(C) Schematic of the $CPAP_{long}$ construct.

(D) Kymograph of microtubule growth at the plus (+) end from a rhodamine-GMPCPP seed with 100 nM CPAPlong. Scale bars, 2 μm (horizontal) and 60 s (vertical).

(E-G) Microtubule plus-end growth rates, catastrophe and rescue frequencies in the presence of rhodamine-tubulin alone or together with CPAPmini-GFP or $CPAP_{long}$-GFP. Error bars represent SEM.

(H) Representative dual-color kymographs showing microtubule plus end dynamics for microtubules grown in the presence of rhodamine-tubulin together with the indicated $CPAP_{mini}$ variants.

Figure S3

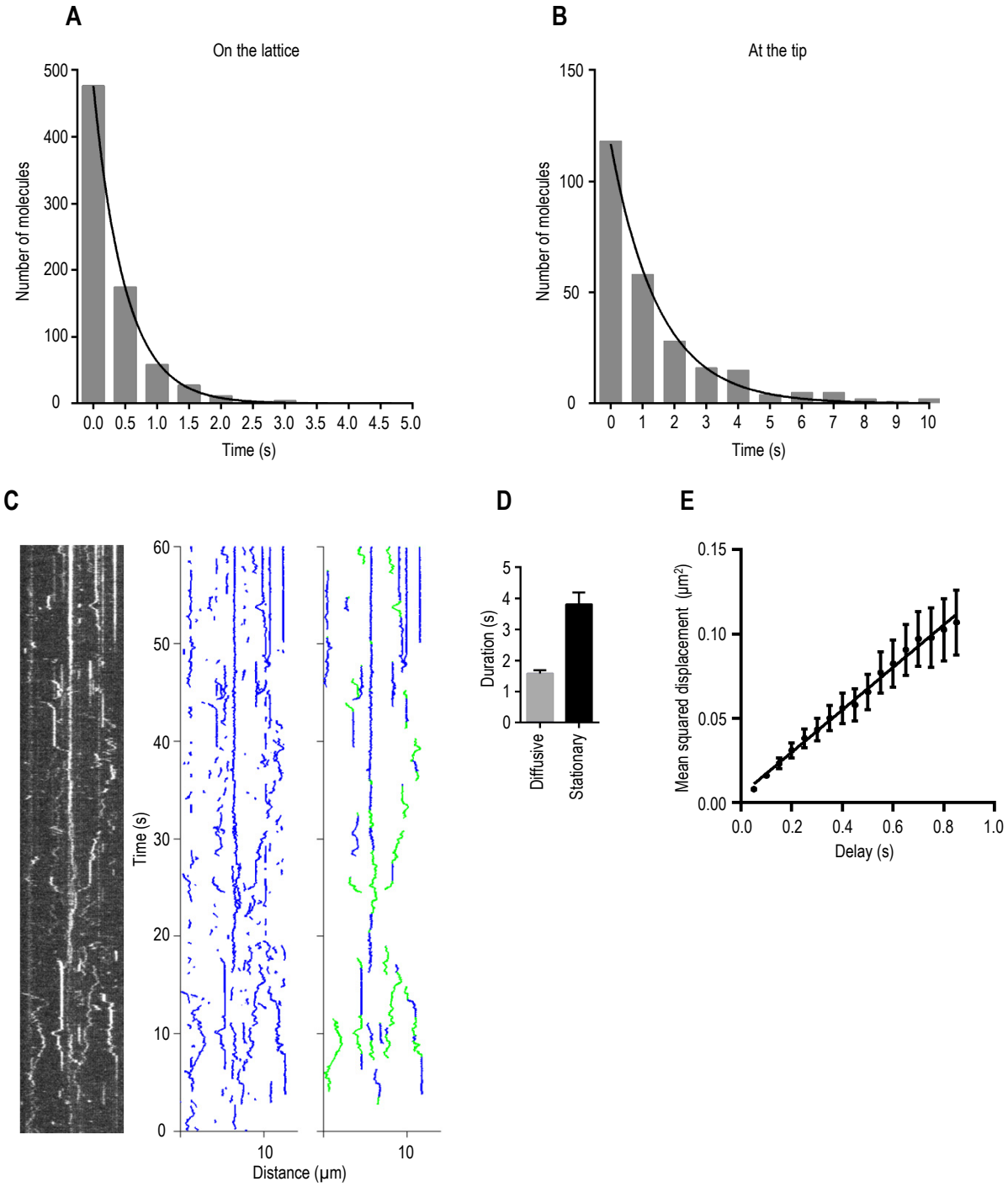
A
On the lattice
Number of molecules
Time (s)
B
At the tip
Number of molecules
Time (s)
C
Time (s)
Distance (μm)
D
Duration (s)
Diffusive
Stationary
E
Mean squared displacement (μm²)
Delay (s)

Figure S3, related to Figure 4. Characterization of $CPAP_{mini}$ single molecule behavior at the tip and on the lattice of dynamic microtubules.

(A-B) Exponential fits of the distributions of dwell times on the microtubule lattice (A) and at the tip (B) for single molecules of $CPAP_{mini}$-GFP.

(C) Representative kymograph illustrating $CPAP_{mini}$-GFP movement on a microtubule (left), corresponding reconstructed tracking results of individual molecules (n=192) (middle), the same tracks filtered for duration (>1.5 s) and color coded depending on the motion behavior: stationary (blue) and diffusive (green) segments (n=29) (right).

(D) Average duration of stationary and diffusive stages of $CPAP_{mini}$-GFP motion (n=134, n=139).

(E) Average mean squared displacement of the diffusive fragments of tracks shown in (C); the line represents linear fit. Error bars represent SEM.

Figure S4

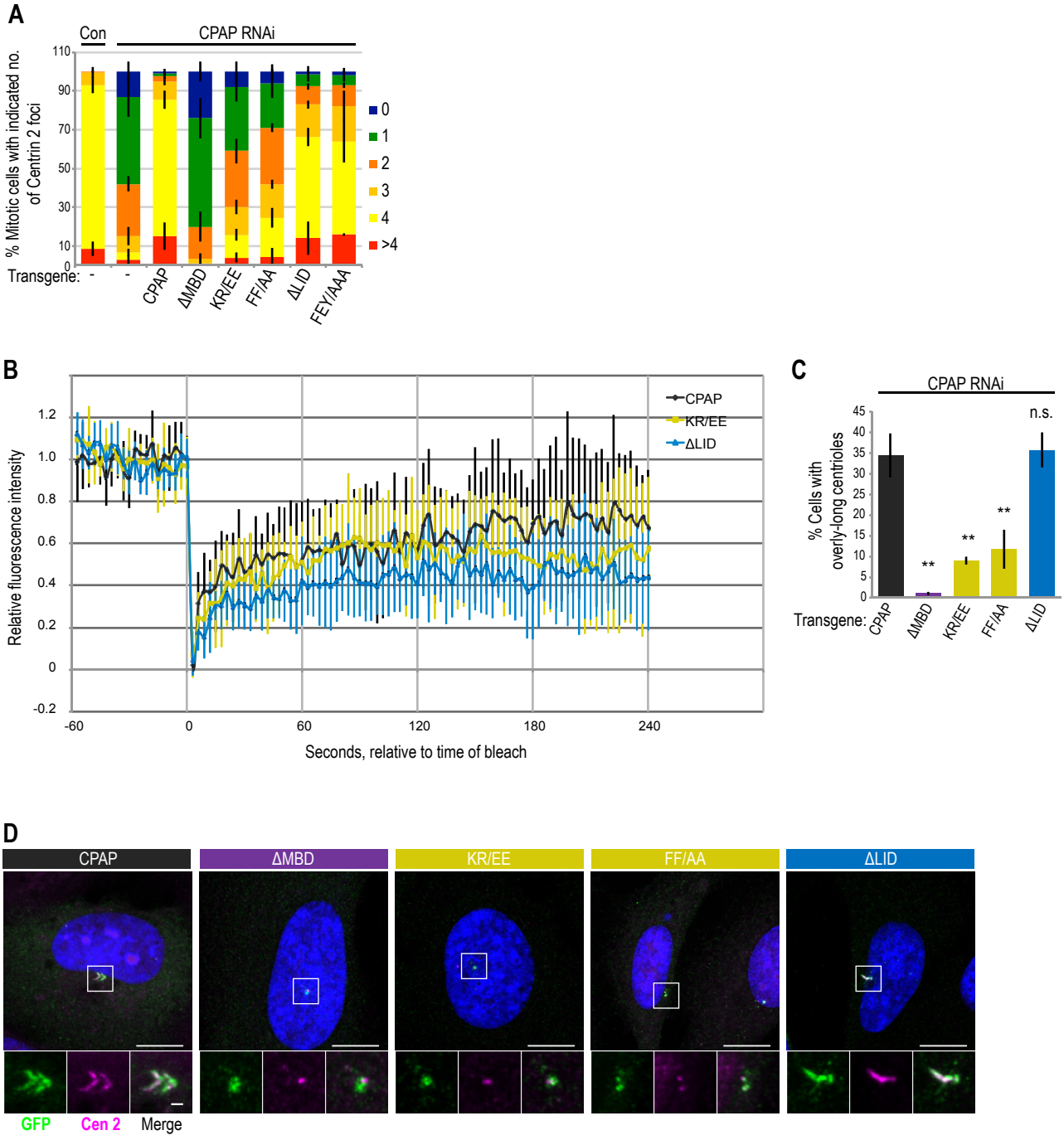
A
Con
CPAP RNAi
% Mitotic cells with indicated no. of Centrin 2 foci
110
90
70
50
30
10
0
0
1
2
3
4
>4
Transgene:
-
-
CPAP
ΔMBD
KR/EE
FF/AA
ΔLID
FEY/AAA
B
Relative fluorescence intensity
1.2
1.0
0.8
0.6
0.4
0.2
0
-0.2
-60
0
60
120
180
240
Seconds, relative to time of bleach
CPAP
KR/EE
ΔLID
C
CPAP RNAi
% Cells with overly-long centrioles
45
40
35
30
25
20
15
10
5
0
n.s.
**
**
**
Transgene:
CPAP
ΔMBD
KR/EE
FF/AA
ΔLID
D
CPAP
ΔMBD
KR/EE
FF/AA
ΔLID
GFP
Cen 2
Merge

Figure S4, related to Figure 5. CPAP SAC domain and MBD, but not the LID domain, are required for centriole over-elongation

(A) Centrin 2 foci scored in mitotic cells expressing the indicated YFP-CPAP variants and depleted of endogenous CPAP by RNAi. Same experiment as shown in Figure 5I, but with all categories displayed. Error bars show the standard deviation of at least 3 experimental replicates, n>100 cells for each sample.

(B) U2OS FlpIn TREX cell lines conditionally expressing indicated YFP-CPAP variants subjected to CPAP RNAi and transgene induction for 72 hours before FRAP analysis. Graph shows mean values, normalized to the mean of the averaged pre-bleach frames for each sample. N = 11 (wild type CPAP and KR/EE), and n = 13 (ΔLID). Time relative to bleach indicated in seconds. Error bars indicate the standard deviation for each time point.

(C, D) U2OS episomal cell lines conditionally expressing indicated GFP-CPAP variants and depleted of endogenous CPAP using RNAi were fixed and stained with anti-GFP and anti-Centrin 2 antibodies 72 hours after RNAi and transgene induction. Scale bar, 10 μm, and 1 μm in insets. Boxes indicate enlarged regions. (C) Proportion of cells with overly long centrioles amongst cells that contain at least one centriole. Note that in all conditions where cells harbored fewer centrioles (see Figure 6A), overly long centrioles were observed less frequently. Average of 3 experimental replicates shown, n >100 cells per experiment. Error bars show standard deviation. Students' paired two-tailed t-test comparing each cell line to the CPAP wild type control: ** indicates $p<0.01$.

Figure S5

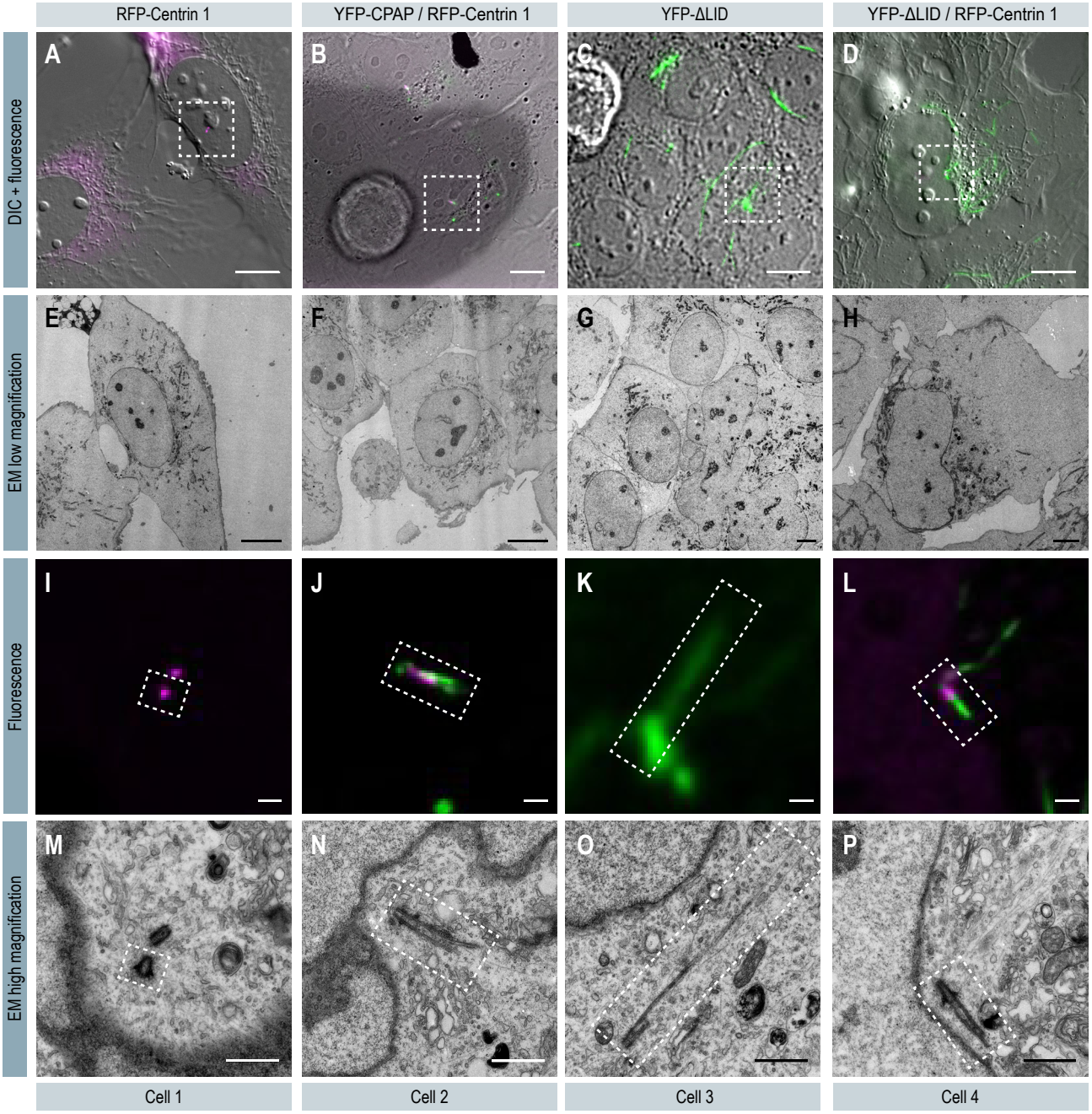
RFP-Centrin 1
YFP-CPAP / RFP-Centrin 1
YFP-ΔLID
YFP-ΔLID / RFP-Centrin 1
DIC + fluorescence
EM low magnification
Fluorescence
EM high magnification
A
B
C
D
E
F
G
H
I
J
K
L
M
N
O
P
Cell 1
Cell 2
Cell 3
Cell 4

Figure S5, related to Figure 7. Correlative light and electron microscopy of cells expressing YFP-CPAP and YFP- ΔLID

(A-D) Differential interference microscopy (DIC) and fluorescence (YFP, RFP, or both) images of the cells shown in Figure 7. Scale bar, 10 μm. Boxes indicate regions shown in I-P.

(E-H) Corresponding low magnification electron microscopy (EM) images of the above cells of interest. Scale bars, 10 μm.

(I-L) High magnification fluorescence images of the regions of interest indicated in (A, E, I, M). Scale bar, 1 μm. Boxes indicate regions shown in Figure 7.

(M-P) High magnification EM images of the regions shown in (C, G, K, O). Scale bars, 1 μm. Boxes indicate regions shown in Figure 7.

Figure S6

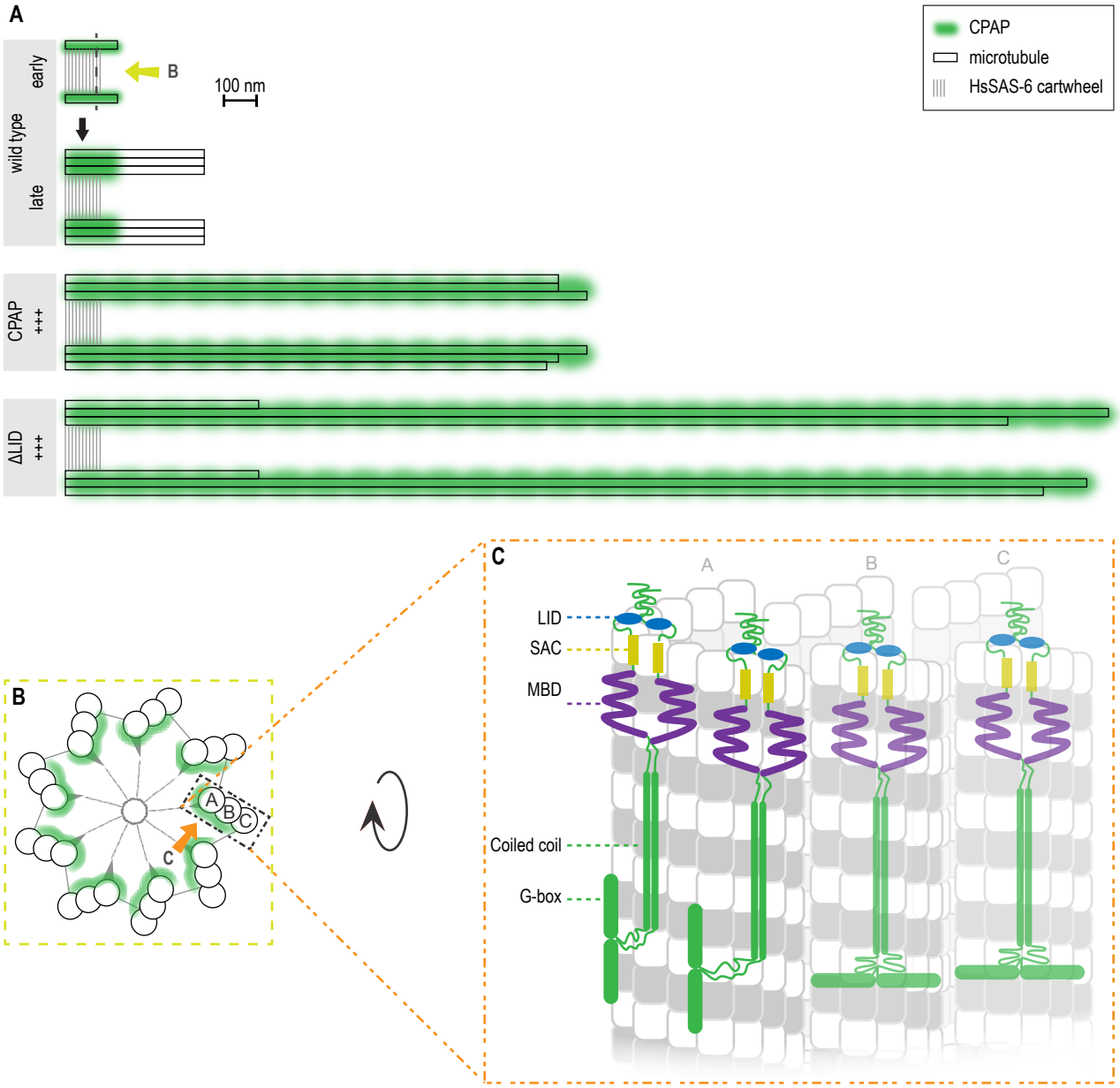
A
wild type
early
late
B
100 nm
CPAP
microtubule
HsSAS-6 cartwheel
CPAP +++
ΔLID +++
B
A
B
C
C
A
B
C
LID
SAC
MBD
Coiled coil
G-box

Figure S6, related to Figure 7. Working model of CPAP's mechanism of action in the context of centrioles.

(A) CPAP (green) is recruited after the assembly of the HsSAS-6-containing cartwheel (gray lines) and the first microtubule (black rectangle). At these early stages of procentriole formation, CPAP is located in the region of the cartwheel and extends slightly more distally. It is during these early stages that CPAP is expected to normally exert its regulation of centriolar microtubule growth. At later stages, CPAP remains in the proximal region of the wild type centriole. Upon overexpression of CPAP (CPAP +++), excess protein localizes along the full length of the centriole, causing over-elongation of centriolar microtubules and the entire distal centriole structure that contains Centrins 1 and 2, and POC5. Overexpression of CPAP-ΔLID (ΔLID +++) results in abnormally elongated centriolar microtubules, which are longer, on average, than the overly-long centrioles observed upon CPAP overexpression, more variable in length, and also lack distal centriole markers such as Centrin and POC5. We refer to these structures as centriole fibers. Light green arrow indicates the direction of view for panel B.

(B) Schematic of a cross section of the centriole looking at the cartwheel-containing region from the distal end. A, B, and C indicate one triplet microtubules. Green indicates the expected position of CPAP, and the orange arrow the direction of view for panel C.

(C) View of the inside surface of a centriolar microtubule triplets with a schematic representation of the position of CPAP dimers (green). CPAP domains are labeled. CPAP dimers located at the tip of the microtubules have their LID domains bound at the end of the β-tubulin subunit, therefore restricting binding of new tubulin dimers to the growing microtubule plus end. CPAP dimers located further down the lattice no longer have their LID domains engaged with tubulin dimers, as the binding interface is occluded, but the SAC and MBD regions still interact with microtubules (not shown). Note that the G-box of the CPAP dimers located on the left are facing inwards the centriole to denote its known interaction with STIL. Note also that whether CPAP is present on all three microtubules in the triplet, and, if so, in how many copies, is not known at present.

Table S1, related to Figures 1, 2, 3 and 5. Constructs used in this study.

Constructs used for structural and biophysical studies	
PN2-3	HsCPAP 311-422
PN2-3s	HsCPAP 319-394
FF/AA	PN2-3 F375A F385A
KR/EE	PN2-3 K377E R378E
FEY/AAA	PN2-3 F338A E399A Y341A
LIDp	PN2-3 311-372
SACp	PN2-3 370-386
Constructs used for in vitro reconstitution studies	
$CPAP_{mini}$	HsCPAP 311-607 GCN4-TEV-eGFP
$CPAP_{mini}$ ΔPN2-3	$CPAP_{mini}$ D311-421
$CPAP_{mini}$ ΔLID	$CPAP_{mini}$ D311-369
$CPAP_{mini}$ FF/AA	$CPAP_{mini}$ F375A F385A
$CPAP_{mini}$ KR/EE	$CPAP_{mini}$ K377E R378E
$CPAP_{mini}$ FEY/AAA	$CPAP_{mini}$ F338A E399A Y341A
$CPAP_{mini}$ ΔMBD	$CPAP_{mini}$ D423-607
$CPAP_{long}$	HsCPAP 312-1053 eGFP
Constructs used for in cellulo studies	
CPAP	HsCPAP
CPAP ΔLID	CPAP D337-350
CPAP FF/AA	CPAP F375A F385A
CPAP KR/EE	CPAP K377E R378E
CPAP ΔMBD	CPAP D423-607

Table S2, related to Figure 1. X-Ray Data Collection and Refinement Statistics.

Data Collection[a]	
Wavelength, Å	1
Space group	P 1 21 1
Resolution range, Å[b]	51.2 - 2.2 (2.28 - 2.2)
Unit cell a, b, c (Å) a, b, g (°)	61.08 85.34 98.69 90 91.77 90
No. of observed reflections	343192 (34254)
No. of unique reflections	51516 (5113)
Mean I/sigma(I)	18.11 (3.19)
R-merge	0.07782 (0.7067)
R-meas	0.09149
$CC_{1/2}$[c]	0.999 (0.87)
CC*	1 (0.964)
Refinement	
R-work	0.1744 (0.2656)
R-free	0.2197 (0.3144)
Number of Macromolecules	7716
Number of Ligands	90
Number of Waters	476
Number of Protein residues	990
RMS(bonds) (Å)	0.021
RMS(angles) (°)	1.03
Ramachandran favored (%)[d]	98
Ramachandran outliers (%)[d]	0.1
B-factors	
Average B-factor	46.57
Macromolecules	46.94
Ligands	35.26
Solvent	42.77

[a] Highest resolution shell statistics are in parentheses.
[b] Resolution cutoffs were chosen based on $CC_{1/2}$ and Mean I/sigma(I) (Karplus and Diederichs, 2012)
[c] As defined by Karplus and Diederichs (Karplus and Diederichs, 2012)
[d] As defined by MolProbity (Davis et al., 2004)

Table S3, related to Figure 4. Characteristics of $CPAP_{mini}$-GFP motion.

Parameter	Mean ± SEM
Average duration of stationary fragment (s)	1.58 ± 0.01
Average duration of diffusive motion (s)	3.81 ± 0.38
Fraction of time spent in diffusive motion (%)	19.7
Diffusion coefficient ($\mu m^2/s$)	0.0257 ± 0.0004
Total number of tracks before filtering	5130
Total number of tracks after filtering	550
Total number of kymographs analyzed	37

Supplemental Experimental Procedures

Protein and peptide preparation

The PN2-3 domain of human CPAP (residues 311-422) and its shorter variant PN2-3s (residues 319-394) were PCR amplified form a *Hs*CPAP clone (Kitagawa et al., 2011) and inserted into the PSTCm1 vector (Olieric et al., 2010) with a N-terminal 6xHis-tag. The DARPin D1 (Pecqueur et al., 2012) was synthesized (GENEWIZ Inc.) and cloned in a T7 pET-based expression vector (Kammerer et al., 1998) with a N-terminal 6xHis-tag. The various CPAP constructs and mutants used in the study are described in Table S1. All PN2-3 mutants were obtained by PCR based mutagenesis. All clones were sequence verified.

Standard protein expression was carried out in the *E. coli* strain BL21(DE3) by induction with 1 mM IPTG at 20 °C. Cells were lysed in a lysis buffer containing 50 mM Tris-HCl, pH 7.5, supplemented with 500 mM NaCl, 10% Glycerol, 10 mM imidazole, 1 mM beta-mercaptoethanol and protease inhibitor cocktail (Roche). Proteins were purified by IMAC using HiTrap Ni-NTA columns (GE Healthcare) followed by size exclusion chromatography on a Superdex 16/60 S75 column. SACp was prepared synthetically using standard peptide synthesis methodology.

Crystallization and structure determination

Bovine brain tubulin was purchased from the Centro de Investigaciones Biológicas (Microtubule Stabilizing Agents Group), CSIC, Madrid, Spain. The flexible C-terminal tails of tubulin were cleaved using subtilisin as described previously (Knipling et al., 1999). Briefly, tubulin was buffer exchanged using a PD-10 desalting column (GE Healthcare) to a buffer containing 10 mM MES pH 6.9, 0.1 mM $MgCl_2$, 0.1 mM EGTA and 1mM of GTP. Subtilisin (Sigma Cat. no. P8038) was added in a weight ratio of 1:100 to a tubulin solution (3 mg/ml) and incubated for 45 minutes at 25 °C. Cleavage was stopped by adding 1 mM PMSF. The reaction mixture was further incubated on ice for 30 minutes followed by centrifugation for 30 minutes at 300,000 x g using an MLA-130 rotor (Beckman Coulter). The supernatant was collected and cleavage efficiency was accessed by a Coomassie stained 7.5% SDS PAGE (Banerjee et al., 2010). The cleaved tubulin was buffer-exchanged to BRB80 (PIPES-KOH, pH 6.8, supplemented with 80 mM, 1 mM $MgCl_2$, 1 mM EGTA) using a PD-10 desalting column (GE Healthcare).

Equimolar amounts of D1, PN2-3 and subtilisin-treated tubulin were mixed and the PN2-3-tubulin-D1 complex was concentrated to ~20 mg/ml using a Centriprep device (Mw cutoff 5 kDa; Amicon). PN2-3-tubulin-D1 samples were complemented with 0.2 mM GDP, 1 mM Colchicine and 5 mM DTT before setting up sitting drop vapor diffusion crystallization trials. Crystals were obtained in a condition containing 20% PEG 550 mono methyl ether (MME) and 0.1 M MES, pH 6.5. Precipitant solution supplemented with 10% glycerol was used as a cryo-protectant for freezing crystals. X-ray diffraction data were collected at 100K at beamline X06DA at the Swiss Light Source (Paul Scherrer Institut, Villigen, Switzerland), and were then processed and merged with XDS (Kabsch, 2010).

The PN2-3-tubulin-D1 structure was solved by molecular replacement using the αβ-tubulin-D1 complex structure as a search model (PDB ID 4DRX) and the program Phaser provided in the Phenix software suite (McCoy et al., 2007). The models were first refined with rigid body refinement and simulated annealing refinement in Phenix (Adams et al., 2010). In the refined structure, the difference electron density for PN2-3 allowed us to model the specific residues of the SAC box using Coot (Emsley and Cowtan, 2004). The resulting model was refined by iterative cycles of model building in coot and refinement in Phenix. The quality of the structures was assessed with MolProbity (Chen et al., 2010) and figures were prepared using PyMOL (The PyMOL Molecular Graphics System, version 1.4.1; Schrödinger, LLC). Data collection and refinement statistics are given in Table S2.

ITC experiments

For exchanging the nucleotide of tubulin, bovine brain tubulin was buffer exchanged to a buffer containing 80 mM PIPES-KOH, pH 6.8, supplemented with 1mM EDTA using a PD-10 desalting column (GE Healthcare). 2 mM of GDP, GTP or GMPCPP was added to the samples that were incubated on ice for 10 minutes. Excess nucleotide was removed by another step of buffer exchange using a PD-10 desalting column pre-equilibrated with BRB80 buffer supplemented with 0.5 mM TCEP. PN2-3 variants were buffer exchanged to BRB80 buffer supplemented with 0.5 mM TCEP by overnight dialysis at 4°C.

Standard ITC experiments were performed at 25 °C using an ITC200 system (Microcal). 0.1–0.4 mM PN2-3 variants in the syringe were injected step-wise into a 10-20 μM tubulin solution in the cell. Experiments with tubulin-D1 in the presence of Eribulin (Eisai Co., Ltd) and Maytansine (National Institutes of Health, Open

Chemical Repository Collection) were obtained by incubating equimolar amounts of tubulin and ligand at 4 °C for 15 minutes before setting up the ITC experiment. The resulting heats were integrated and fitted in Origin (OriginLab) using the standard 'one set of sites' model provided by the software package.

Protein purification for in vitro reconstitution assays

$CPAP_{long}$–GFP and $CPAP_{mini}$-GFP variants used in the *in vitro* reconstitutions assays (Table S1) were purified from HEK293T cells using the Strep(II)-streptactin affinity purification. Cells were harvested 2 days post transfection. Cells from a 25 cm dish were lysed in 500 µl of lysis buffer (50 mM HEPES, 300 mM NaCl and 0.5% Triton X-100, pH 7.4) supplemented with protease inhibitors (Roche) on ice for 10 minutes. The supernatant obtained from the cell lysate after centrifugation at 16,000 x g for 20 minutes was incubated with 40 µl of StrepTactin Sepharose beads (GE) for 1 hour. The beads were washed 3 times in the lysis buffer without the protease inhibitors. The protein was eluted with 40 µl of elution buffer (50 mM HEPES, 150 mM NaCl, 1 mM $MgCl_2$, 1 mM EGTA, 1 mM dithiothreitol (DTT), 2.5 mM d-Desthiobiotin and 0.05% Triton X-100, pH 7.4). Purified proteins were snap-frozen and stored at -80 °C. Bacterially expressed mCherry-EB3 was produced as described previously (Montenegro Gouveia et al., 2010) and mCherry-CAMSAP3 was produced in HEK293T cells as described previously (Jiang et al., 2014).

In vitro reconstitution assay

Reconstitution of microtubule growth dynamics *in vitro* was performed as described previously (Montenegro Gouveia et al., 2010). GMPCPP microtubule seeds (70% unlabeled tubulin, 18% biotin tubulin and 12% rhodamine tubulin) were prepared as described before (Gell et al., 2010). Flow chambers, assembled from plasma-cleaned glass coverslips and microscopic slides were functionalized by sequential incubation with 0.2 mg/ml PLL-PEG-biotin (Susos AG, Switzerland) and 1 mg/ml NeutrAvidin (Invitrogen) in MRB80 buffer (80 mM piperazine-*N*,*N*[prime]-bis(2-ethanesulfonic acid), pH 6.8, supplemented with 4 mM $MgCl_2$, and 1 mM EGTA. The microtubule seeds were attached to coverslips through biotin-NeutrAvidin interactions. Flow chambers were further blocked with 1 mg/ml κ-casein. The reaction mix with or without $CPAP_{mini}$ proteins (MRB80 buffer supplemented with 15 µM porcine brain tubulin, 0.5 µM rhodamine-tubulin, 50 mM KCl, 1 mM guanosine triphosphate, 0.2 mg/ml κ-casein, 0.1% methylcellulose, and oxygen scavenger mix [50 mM glucose, 400 µg/ ml glucose oxidase, 200 µg/ml catalase, and 4 mM DTT]) was added to the flow chamber after centrifugation in an Airfuge for 5 minutes at 119,000 × *g*. For experiments in the presence of EB3, concentration of mCherry-EB3 was 20 nM and rhodamine-tubulin was excluded from the assay. Rhodamine-tubulin was also excluded from the assay with $CPAP_{mini}$-GFP and mCherry-CAMSAP3. The flow chamber was sealed with vacuum grease, and dynamic microtubules were imaged immediately at 30 °C using Total Internal Reflection Fluorescence (TIRF) microscopy. All tubulin products were from Cytoskeleton Inc.

TIRF microscopy

The in vitro reconstitutions assays were imaged on a TIRF microscope setup as described in (Mohan et al., 2013) or on an $iLas^2$ TIRF setup. In brief, we used an inverted research microscope Nikon Eclipse Ti-E with the perfect focus system, equipped with Nikon CFI Apo TIRF 100x 1.49 N.A. oil objective and controlled with MetaMorph 7.7.5 software (Molecular Devices). The microscope was equipped with TIRF-E motorized TIRF illuminator modified by Roper Scientific France/PICT-IBiSA, Institut Curie. To keep the in vitro samples at 30 °C, a stage top incubator model INUBG2E-ZILCS (Tokai Hit) was used. For excitation, 491 nm 100 mW Calypso (Cobolt) and 561 nm 100 mW Jive (Cobolt) lasers were used. We used ET-GFP 49002 filter set (Chroma) for imaging of proteins tagged with GFP or ET-mCherry 49008 filter set (Chroma) for imaging of proteins tagged with mCherry. Fluorescence was detected using an EMCCD Evolve 512 camera (Roper Scientific) with the intermediate lens 2.5X (Nikon C mount adapter 2.5X) or using the CoolSNAP HQ2 CCD camera (Roper Scientific) without an additional lens. In both cases the final magnification was 0.063 µm/pixel.

$ILas^2$ system (Roper Scientific, Evry, France) is a dual laser illuminator for azimuthal spinning TIRF illumination and with a custom modification for targeted photomanipulation. This system was installed on the Nikon Ti-E microscope with the perfect focus system, equipped with 150 mW 488 nm laser and 100 mW 561 nm laser, 49002 and 49008 Chroma filter sets, EMCCD Evolve mono FW DELTA 512x512 camera (Roper Scientific) with the intermediate lens 2.5X (Nikon C mount adapter 2.5X), CCD camera CoolSNAP MYO M-USB-14-AC (Roper Scientific) and controlled with MetaMorph 7.8.8 software (Molecular Device). To keep the in vitro samples at 30°C, a stage top incubator model INUBG2E-ZILCS (Tokai Hit) was used. The final resolution using Evolve EMCCD camera was 0.065 □m/pixel, using CoolSNAP Myo CCD camera it was 0.045 µm/pixel.

Analysis of microtubule plus end dynamics in vitro

Kymographs were generated using the ImageJ plugin KymoResliceWide (http://fiji.sc/KymoResliceWide). Microtubule dynamics parameters were determined from kymographs using an optimized version of the custom made JAVA plug in for ImageJ as described previously (Jiang et al., 2014; Montenegro Gouveia et al., 2010; Taylor, 1997). ~100-200 microtubule growth events were analyzed per condition.

Intensity analysis for $CPAP_{mini}$ along microtubules

Intensity profiles extraction and alignment of rhodamine-tubulin and $CPAP_{mini}$ were performed using a custom written Matlab routine. First, we obtained the average intensity of microtubule profile along a 4-pixel wide line using the rhodamine-tubulin channel. The same line was used to obtain an intensity profile in the $CPAP_{mini}$ (GFP) channel. After background subtraction, each intensity profile $I(x)$ was normalized:

$$I_{norm}(x) = \frac{I(x) - I_{\min}}{I_{\max} - I_{\min}} \cdot 100\% \; \mathrm{I_{normalized}} = \left(\frac{\mathrm{I\text{-}I_{min}}}{\mathrm{I_{max}\text{-}I_{min}}}\right) \mathrm{xd}$$

with respect to the maximum and minimum intensity values along the whole profile. The normalized intensity profiles of different microtubules were aligned so that the plus end tip position was at the origin of the coordinates (Figure 3C). The plus end position was determined by fitting the rhodamine-tubulin profile to a Gaussian survival function using equation:

$$I_{norm}(x) = \frac{1}{2} I_{MT} erfc\left(\frac{x - x_{PF}}{\sqrt{2}\sigma_{PF+PSF}}\right) + I_{BG}$$

where erfc is the complimentary error function, I_{MT} and I_{BG} are average intensities of the microtubule and the background, x_{PF} is the position of plus end tip and σ_{PF+PSF} is the standard deviation of the microtubule tip taper combined with the one for the microscope point spread function.

Single-molecule fluorescence intensity analysis of $CPAP_{mini}$

Sample preparation for the fluorescence intensity analysis was performed by immobilizing diluted GFP or $CPAP_{mini}$-GFP proteins non-specifically to the plasma cleaned glass coverslips in flow chambers. After protein addition the flow chambers were washed with MRB80 buffer, sealed with vacuum grease and immediately imaged with a TIRF microscope. 10-20 images of previously unexposed coverslip areas were acquired with 100 ms exposure time and low laser power. GFP and $CPAP_{mini}$-GFP were located in different chambers of the same coverslip, so the same imaging conditions could be preserved. Single molecule fluorescence spots were detected and fitted with 2D Gaussian function using custom written ImageJ plugin DoM_Utrecht (https://github.com/ekatrukha/DoM_Utrecht). The fitted peak intensity values were used to build fluorescence intensity histograms.

Single molecule diffusion and kinetics analysis

The study of single molecule kinetics of $CPAP_{mini}$ at the tip and lattice of dynamic microtubules was performed in the presence of 100 nM $CPAP_{mini}$-mCherry, 5 nM $CPAP_{mini}$-GFP and rhodamine tubulin. Kymographs were generated for each microtubule over 60 seconds with 50 millisecond intervals. The residence times at the microtubule tip and lattice were manually obtained from kymographs. Histograms of times for both conditions were fitted to a single exponential decay function in GraphPad Prism 6. The reported mean residence time at the lattice and tip were obtained from these fits. The mean residence time was corrected for photo bleaching as described (Helenius et al., 2006). The characteristic time constant of photobleaching was estimated by fitting the total field of view intensity of $CPAP_{mini}$ movies over time to a single exponential decay function. The value of averaged photobleaching time constant over 15 movies was used for correction.

Coordinates of individual fluorescent spots of $CPAP_{mini}$-GFP diffusing along microtubule were derived from the detection performed using the ImageJ plugin DOM_Utrecht as described above. Detections were linked to 2D tracks using nearest neighbor linking algorithm of the same plugin with a search radius of 0.5-1 μm. Coordinates

of all time points of all the tracks along the same microtubule were fitted to a straight line and subsequently projected on it resulting in 1D tracks. Only tracks longer than 1.5 seconds were considered. Mean squared displacement (MSD) analysis was performed using msdanalyzer Matlab routine (Tarantino et al., 2014). To separate the periods of stationary and diffusive motion for each track MSD (τ) was calculated by internal averaging for a sliding window of 30 frames. The first 7 point (excluding zero) were used to fit $MSD(\tau)=0.5D\tau+b$, with D termed the 1D diffusion coefficient and b as a localization precision error. For each fit we calculated the coefficient of determination R^2 characterizing the quality of fit. Track fragments where R^2 was above the threshold of 0.7 were considered as "diffusing state", since the sliding window MSD fitted well with linear dependence (green tracks in Figure S3C, right panel). The rest of the track was considered being in the "stationary state" (blue fragments in Figure S3C, right panel). The diffusion coefficient reported in Supplementary Table S3 was calculated by averaging all D values from all fits where $R^2>0.7$ (n=8959).

$CPAP_{mini}$ molecule counting at microtubule tips

To determine the number of molecules of $CPAP_{mini}$ at a microtubule tip, we immobilized single molecules of $CPAP_{mini}$ onto the coverslip of one of the flow chambers and performed the *in vitro* reconstitution assay in the adjacent chamber of the same coverslip. Images of unbleached $CPAP_{mini}$ single molecules were acquired first and using the same imaging/illumination conditions, time lapse imaging was performed on the *in vitro* assay with $CPAP_{mini}$, using 100 ms exposure and 2 second intervals for 5 minutes. The plus end localized $CPAP_{mini}$ molecules were manually located in each frame and fitted with 2D Gaussian, the amplitude of which was used for the intensity analysis. To build the distributions of $CPAP_{mini}$ molecule numbers at the microtubule tip, each $CPAP_{mini}$ intensity value at the microtubule plus end was normalized by the average $CPAP_{mini}$ single molecule intensity from the adjacent chamber.

Statistical Analysis

The relative standard error for catastrophe frequency was calculated as described (Taylor, 1997). The relative standard error of mean rescue frequency in the experiments with $CPAP_{mini}$ constructs was calculated in the same way as the standard error of the mean catastrophe frequency, i.e. $SE_r = \bar{f}_r \frac{SE_{t_{sh}}}{\bar{t}_{sh}}$, where $\bar{f}_r, \bar{t}_{sh}$ are average values and $SE_{f_r}, SE_{t_{sh}}$ are standard errors of rescue frequency and shortening time respectively. The number of observed rescue events for control was relatively small as compared to the catastrophes, so we assumed that they follow a Poisson distribution. The standard deviation of the rescue frequency was calculated as the square root of its mean value and the standard error was calculated according to $SE_{f_r} = \frac{\sqrt{\bar{f}_r}}{\sqrt{N_r}}$, where $\bar{f}_r$ and SE_{f_r} are the average and the standard error of the rescue frequency and N_r is the number of rescues (Smal et al., 2009).

Generation of expression vectors for cell biology

A cDNA encoding siRNA resistant CPAP was cloned into pENTR 1A, as previously described (Kitagawa et al., 2011). This vector was used for site directed mutagenesis reactions to produce KR/EE and FF/AA mutations using Quikchange Site Directed Mutagenesis kit (Agilent). Deletions ΔLID and ΔMBD were generated using Phusion polymerase (NEB). For deletion mutants, linear PCR products were generated with 10 bp overlapping regions and ligated using CloneEZ (GenScript). Entry vectors were then used in LR Clonase reactions (Invitrogen) with pEBTet-EGFP-GW (Kitagawa et al., 2011) or pcDNA5FRT/TO-YFP-GW (gift from Zuzana Hořejší) to produce expression vectors. All Entry clones were sequence-verified.

Cell culture, transfections, cell line generation, and siRNAs

U2OS cells were cultured in high-glucose DMEM with GlutaMAX (Invitrogen) supplemented with 10% fetal calf serum (FCS) in a humidified 5% CO_2 incubator at 37 °C. To generate inducible cell lines with the pEBTet-EGFP vector, cells were transfected with the appropriate vectors using Lipofectamine 2000 (Invitrogen) and selected using 1 μg/ml puromycin 24 hours after transfection, as previously described (Kitagawa et al., 2011). For generating stable integrated cell lines, we used a U2OS FlpIn TREX cell line, a gift from Erich Nigg (Arquint and Nigg, 2014). U2OS FlpIn TREX cells were transfected using Lipofectamine 2000 with a 3:1 ratio

of pcDNA5-FRT/TO-YFP-CPAP vectors:pOG44 (Invitrogen Flp-In System). Cells were selected using 100 µg/ml Hygromycin B and 10 µg/ml Blasticidin (both from InvivoGen) for 1-2 weeks, until all untransfected cells were dead. For both types of cell line, 1 µg/ml doxycycline was used to induce transgene expression (Sigma-Aldrich). CPAP RNAi was carried out at 60 nM as previously described (Kitagawa et al., 2011) and Stealth siRNA Negative Control Lo GC was used as a negative control, also at 60 nM. Unless otherwise indicated, RNAi was carried out for 72 hour before fixation of the cells, with simultaneous induction of transgene expression with 1 µg/ml Doxycycline. Note that cells expressing KR/EE often exhibited large globular YFP aggregates, but never microtubule decoration, perhaps explaining the absence of centrosomal fibers in this mutant compared to FF/AA (see Figure 6A).

Correlative light and electron microscopy (CLEM)

Cells were cultured on glass coverslips coated on one side with a 3 nm thick layer of carbon, with an additional layer of 10 nm thickness to reveal a gridded pattern with a coordinate system of letters for locating the cell of interest by light microscopy, and also once the cells were resin embedded. Endogenous CPAP was depleted by RNAi for 72 hours, simultaneous with induction of the transgene. For dual marker experiments, cells were transfected with a tagRFP-Centrin 1 expression vector 16 hours prior to fixation (Keller et al., 2014). Cells were fixed in a solution of 0.1 % glutaraldehyde and 2.0 % paraformaldehyde in 0.1 M phosphate buffer, pH 7.4, for 2 hours, then washed thoroughly with cacodylate buffer (0.1 M, pH 7.4), and imaged by wide field light microscopy using a Zeiss Plan-Apochromat 63 x oil-immersion objective, NA 1.40. Z-sections were imaged at an interval of ~0.3 µm. Fluorescence images shown in Figure 7 are single plane images deconvolved using Huygens Core 15.10 software (Scientific Volume Imaging, SVI) through the web interface Huygens Remote Manager. A theoretical Point Spread Function (PSF) was used in combination with the "Classic Maximum Likelihood Estimation" algorithm, an automatic background estimation and stopping criteria of 40 iterations and 0.1 quality change. The deconvolution settings and signal to noise ratios were set according to SVI's recommendations. Immediately after imaging, samples were post-fixed for 40 minutes in 1.0 % osmium tetroxide, then 30 minutes in 1.0% uranyl acetate in water, before being dehydrated through increasing concentrations of alcohol and then embedded in Durcupan ACM resin (Fluka, Switzerland). The coverslips were then placed face down on a glass slide coated with mold releasing agent (Glorex, Switzerland), with approximately 1 mm of resin separating the two. The resin was initially hardened for 12 hours in a 65 °C oven and then the coverslips detached from the resin by immersing them alternately into hot (60 °C) water followed by liquid nitrogen. The smooth resin surface, with the cells embedded, also showed the grid pattern, which was used to locate the region of interest imaged by light microscopy. These regions were mounted on blank resin blocks with acrylic glue and trimmed with glass knives to form a block ready for serial sectioning. Series of between 150 and 300 thin sections (50 nm thickness) were cut with a diamond knife mounted on an ultramicrotome (Leica UC7), and collected onto single-slot, copper grids with a pioloform support film. These sections were contrasted with lead citrate and uranyl acetate, and images taken using an FEI Spirit TEM with Eagle CCD camera. Images of each cell of interest were taken on every section in which it appeared and these images aligned using Photoshop (Adobe). The aligned series was then matched with the light microscopy images to correlate the position of the fluorescent signal with the underlying ultrastructure.

Fluorescence Recovery After Photo-bleaching (FRAP)

Cells were grown in glass bottomed cell culture dishes (Matek) and imaged in a humidified 5% CO_2 incubator at 37 °C in DMEM high glucose medium without phenol red (GE Healthcare), supplemented with 15% FCS, 20 mM HEPES buffer (Gibco), 1 mM sodium pyruvate (Sigma), and Penicillin/Streptomycin (Gibco). We used a Zeiss LSM 710 with an N-Achromat 63x water immersion objective NA 0.90, controlled with Zeiss Zen software to bleach a circular region of 25 pixel diameter (pixel size 0.14 µm) around the centrosome using 10 iterations with the 514 nm laser at 100%, and acquisition of a 60 x 60 pixel region with a pixel dwell time of 2.77 µsec and 2 x averaging. Cells were imaged every 3 seconds, for one minute pre- and 4 minutes post-bleach. Analysis was carried out using Image J, with a plugin to automatically detect a circular region of interest of 15 pixel diameter using a Gaussian blurring factor of 5 and the brightest pixel to center the region of interest. Before measuring fluorescence intensity, the regions of interest were manually curated to ensure that the centrosome was contained within it. All FRAP curves were normalized to the average of the first 20 pre-bleach intensities.

Supplemental References

Adams, P.D.et al. (2010). PHENIX: a comprehensive Python-based system for macromolecular structure solution. Acta Crystallogr. D. Biol. Crystallogr. *66*, 213-221.

Arquint, C. and Nigg, E.A. (2014). STIL microcephaly mutations interfere with APC/C-mediated degradation and cause centriole amplification. Curr. Biol. *24*, 351-360.

Azimzadeh, J., Hergert, P., Delouvee, A., Euteneuer, U., Formstecher, E., Khodjakov, A., and Bornens, M. (2009). hPOC5 is a centrin-binding protein required for assembly of full-length centrioles. J. Cell Biol. *185*, 101-114.

Banerjee, A., Bovenzi, F.A., and Bane, S.L. (2010). High-resolution separation of tubulin monomers on polyacrylamide minigels. Anal. Biochem. *402*, 194-196.

Chen, V.B., Arendall, W.B., III, Headd, J.J., Keedy, D.A., Immormino, R.M., Kapral, G.J., Murray, L.W., Richardson, J.S., and Richardson, D.C. (2010). MolProbity: all-atom structure validation for macromolecular crystallography. Acta Crystallogr. D. Biol. Crystallogr. *66*, 12-21.

Davis, I.W., Murray, L.W., Richardson, J.S., and Richardson, D.C. (2004). MOLPROBITY: structure validation and all-atom contact analysis for nucleic acids and their complexes. Nucleic Acids Res. *32*, W615-W619.

Emsley, P. and Cowtan, K. (2004). Coot: model-building tools for molecular graphics. Acta Crystallogr. D. Biol. Crystallogr. *60*, 2126-2132.

Gell, C.et al. (2010). Microtubule dynamics reconstituted in vitro and imaged by single-molecule fluorescence microscopy. Methods Cell Biol. *95*, 221-245.

Helenius, J., Brouhard, G., Kalaidzidis, Y., Diez, S., and Howard, J. (2006). The depolymerizing kinesin MCAK uses lattice diffusion to rapidly target microtubule ends. Nature *441*, 115-119.

Jiang, K.et al. (2014). Microtubule minus-end stabilization by polymerization-driven CAMSAP deposition. Dev. Cell *28*, 295-309.

Kabsch, W. (2010). XDS. Acta Crystallogr. D. Biol. Crystallogr. *66*, 125-132.

Kammerer, R.A., Schulthess, T., Landwehr, R., Lustig, A., Fischer, D., and Engel, J. (1998). Tenascin-C hexabrachion assembly is a sequential two-step process initiated by coiled-coil alpha-helices. J. Biol. Chem. *273*, 10602-10608.

Karplus, P.A. and Diederichs, K. (2012). Linking crystallographic model and data quality. Science *336*, 1030-1033.

Kitagawa, D., Kohlmaier, G., Keller, D., Strnad, P., Balestra, F.R., Fluckiger, I., and Gönczy, P. (2011). Spindle positioning in human cells relies on proper centriole formation and on the microcephaly proteins CPAP and STIL. J. Cell Sci. *124*, 3884-3893.

Knipling, L., Hwang, J., and Wolff, J. (1999). Preparation and properties of pure tubulin S. Cell Motil. Cytoskeleton *43*, 63-71.

McCoy, A.J., Grosse-Kunstleve, R.W., Adams, P.D., Winn, M.D., Storoni, L.C., and Read, R.J. (2007). Phaser crystallographic software. J Appl Crystallogr. *40*, 658-674.

Mohan, R., Katrukha, E.A., Doodhi, H., Smal, I., Meijering, E., Kapitein, L.C., Steinmetz, M.O., and Akhmanova, A. (2013). End-binding proteins sensitize microtubules to the action of microtubule-targeting agents. Proc. Natl. Acad. Sci. U. S. A *110*, 8900-8905.

Montenegro Gouveia, S.et al. (2010). In vitro reconstitution of the functional interplay between MCAK and EB3 at microtubule plus ends. Curr. Biol. *20*, 1717-1722.

Olieric, N., Kuchen, M., Wagen, S., Sauter, M., Crone, S., Edmondson, S., Frey, D., Ostermeier, C., Steinmetz, M.O., and Jaussi, R. (2010). Automated seamless DNA co-transformation cloning with direct expression vectors applying positive or negative insert selection. BMC. Biotechnol. *10*, 56.

Pecqueur, L., Duellberg, C., Dreier, B., Jiang, Q., Wang, C., Pluckthun, A., Surrey, T., Gigant, B., and Knossow, M. (2012). A designed ankyrin repeat protein selected to bind to tubulin caps the microtubule plus end. Proc. Natl. Acad. Sci. U. S. A *109*, 12011-12016.

Schindelin, J.et al. (2012). Fiji: an open-source platform for biological-image analysis. Nat. Methods *9*, 676-682.

Smal, I., Grigoriev, I., Akhmanova, A., Niessen, W.J., and Meijering, E. (2009). Accurate estimation of microtubule dynamics using kymographs and variable-rate particle filters. Conf. Proc. IEEE Eng Med. Biol. Soc. *2009*, 1012-1015.

Tarantino, N., Tinevez, J.Y., Crowell, E.F., Boisson, B., Henriques, R., Mhlanga, M., Agou, F., Israel, A., and Laplantine, E. (2014). TNF and IL-1 exhibit distinct ubiquitin requirements for inducing NEMO-IKK supramolecular structures. J. Cell Biol. *204*, 231-245.

Taylor, J.R. (1997). An Introduction to Error Analysis. University Science Books, Sausalito).